

Linc-MYH configures INO80 to regulate muscle stem cell numbers and skeletal muscle hypertrophy

Christian Schutt¹, Alix Hallmann¹, Salma Hachim¹, Ina Klockner¹, Melissa Valussi¹, Ann Atzberger², Johannes Graumann³ , Thomas Braun^{1,*}  & Thomas Boettger^{1,**} 

Abstract

Chromatin remodeling complexes have functions in transcriptional regulation and chromosome maintenance, but it is mostly unknown how the function of these normally ubiquitous complexes is specified in the cellular context. Here, we describe that the evolutionary conserved long non-coding RNA linc-MYH regulates the composition of the INO80 chromatin remodeler complex in muscle stem cells and prevents interaction with WDR5 and the transcription factor YY1. Linc-MYH acts as a selective molecular switch *in trans* that governs the pro-proliferative function of the ubiquitous INO80 complex but does not affect its role in maintaining genomic stability. The molecular switch is essential for restricting generation of quiescent MuSCs and proliferation of myoblasts in homeostasis and regeneration. Since linc-MYH is expressed in proliferating myoblasts but not in quiescent MuSCs, we reason that the extent of myoblast proliferation has decisive effects on the size of the quiescent MuSC pool.

Keywords Chromatin remodeler; lincRNA; muscle stem cell proliferation; non-coding RNA function; satellite cell

Subject Categories Chromatin, Transcription & Genomics; RNA Biology; Stem Cells & Regenerative Medicine

DOI 10.15252/embj.2020105098 | Received 25 March 2020 | Revised 20 August 2020 | Accepted 24 August 2020 | Published online 22 September 2020

The EMBO Journal (2020) 39: e105098

Introduction

Skeletal muscle has a remarkable capacity for regeneration, which critically depends on the function of adult muscle stem cells (MuSCs). MuSCs are located on myofibers under the basal lamina and thus are also named satellite cells (Mauro, 1961). MuSCs are readily identified by the expression of the paired-box transcription factor Pax7 (Seale *et al*, 2000; Oustanina *et al*, 2004) and mostly rest in a quiescent state under homeostatic conditions. Upon injury, they become activated followed by proliferation, differentiation, and fusion to myofibers. Some activated MuSCs do not submit to

differentiation during tissue renewal and regeneration but replenish the MuSC pool (Motohashi & Asakura, 2014; Almada & Wagers, 2016). Since inhibition of MuSC proliferation or ablation of MuSCs only has effects on skeletal muscles during regeneration or long-term maintenance, it had been assumed that MuSCs rarely proliferate under baseline conditions (Murach *et al*, 2017; Fukada, 2018; van Velthoven & Rando, 2019). However, recent studies demonstrate that approximately 10% of MuSCs become labeled by EdU over a two-week period, suggesting substantial proliferation of MuSCs even under homeostatic conditions (Pawlikowski *et al*, 2015).

The definitive amount of MuSCs is determined during postnatal development in individual skeletal muscles and remains stable after reaching adulthood, even after multiple rounds of tissue regeneration (White *et al*, 2010; Keefe *et al*, 2015). During aging, the number of MuSCs eventually declines, associated with reduced proliferative capacity of activated MuSCs (Garcia-Prat *et al*, 2013). Up to now, the mechanisms determining the size of the quiescent MuSC stem cell pool during homeostasis and after injury are incompletely understood. Different concepts have been proposed, which are mostly based on the frequency of symmetric and asymmetric cell divisions, either immediately after MuSC activation or during the course of MuSC expansion (Almada & Wagers, 2016). However, it is not clear how this relates to the settlement of satellite cell numbers. Expansion of MuSCs is assumed to strongly depend on the control of external signals, derived from the forming stem cell niche, neighboring stromal cells such as fibroadipogenic progenitor cells, or from infiltrating immune cells stimulating or preventing cellular proliferation and differentiation of muscle cells (Baghdadi & Tajbakhsh, 2018; Wosczyzna & Rando, 2018). Epigenetic mechanisms also directly contribute to the regulation of MuSC expansion aside from their pivotal roles in controlling chromatin condensation and MuSC quiescence (Segales *et al*, 2016; Robinson & Dilworth, 2018). For instance, the PRC2 component Ezh2 maintains a key phase of MuSC expansion (Woodhouse *et al*, 2013), the arginine methyltransferase Prmt5 regulates MuSC expansion by controlling p21 expression (Zhang *et al*, 2015), and HDAC4 directs MuSC proliferation by targeting p21 and Sharp1 (Marroncelli *et al*, 2018). Moreover, HDAC1 is recruited to muscle gene promoters by YY1 as part

¹ Department of Cardiac Development and Remodelling, Max Planck Institute for Heart- and Lung Research, Bad Nauheim, Germany

² Max Planck Institute for Heart- and Lung Research, FACS Service Group, Bad Nauheim, Germany

³ Max Planck Institute for Heart- and Lung Research, Mass Spectrometry Service Group, Bad Nauheim, Germany

*Corresponding author. Tel: +49 60327051102; E-mail: thomas.braun@mpi-bn.mpg.de

**Corresponding author (lead contact). Tel: +49 60327051115; E-mail: thomas.boettger@mpi-bn.mpg.de

of the Ezh2 complex to prevent differentiation and promote proliferation (Caretta *et al*, 2004). The chromatin architecture is also regulated by chromatin remodeling complexes, which either move, eject, or restructure nucleosomes by exchanging histone monomers (Poli *et al*, 2017). Chromatin remodeling complexes do not only regulate gene expression but also fulfill different functions to maintain genome stability. The enormous functional diversity of chromatin remodeler complexes is in part accomplished by changes in their subunit composition. The core complex of chromatin remodelers, which already consists of several subunits, associates with distinct transcription factors that determine localization and activity. For examples, some activities of the INO80 chromatin remodeler depend on interactions with WDR5 (Wang *et al*, 2014; Zhou *et al*, 2016) and YY1 (Cai *et al*, 2007; Vella *et al*, 2012). Dynamic, cell stage-dependent changes in complex composition might be critical to regulate individual modalities of chromatin remodeler complexes with different functions.

Long non-coding (lnc-) RNAs have recently come into focus as regulatory factors that often interact directly with proteins to control their localization and/or activity (Ulitsky & Bartel, 2013; Kopp & Mendell, 2018). Nuclear lncRNAs are frequently involved in the epigenetic control of gene expression by recruiting epigenetic regulators to specific sites in the genome or by serving as scaffolds for the assembly of larger complexes (Quinn & Chang, 2015; Carlevaro-Fita & Johnson, 2019). Since lncRNAs are typically expressed in specific cell types at distinct stages (Cabili *et al*, 2011; Gloss & Dinger, 2016), they might confer cell type specificity to more broadly expressed epigenetic regulators. Here, we investigated the role of lncRNAs for the epigenetic control of MuSC activation, expansion, and muscle regeneration. We screened for lncRNAs that are exclusively expressed at different stages of MuSC proliferation and differentiation and identified the evolutionary conserved linc-MYH, which is co-expressed with the largest myosin cluster in mammals. We found that linc-MYH interacts specifically with functional domains of the INO80 chromatin remodeler complex and controls its composition. Linc-MYH prevents interaction of the INO80 complex with the transcription factor YY1 and the scaffolding protein WDR5. Upregulation of linc-MYH during MuSC proliferation is decisive to limit proliferation of MuSCs and contains the size of the quiescent MuSC pool, thereby preventing myofiber hypertrophy during muscle homeostasis and after regeneration. We propose that Linc-MYH acts as a selective molecular switch for INO80, allowing stage-specific regulation of distinct INO80 activities in MuSCs.

Results

Linc-MYH is confined to the nucleus of proliferating and differentiating MuSCs

To explore the function of lncRNAs that are located in nuclei of MuSCs and hence might be involved in the regulation of epigenetic processes, we used RNA sequencing data obtained from freshly isolated, proliferating and differentiating murine MuSCs (Wust *et al*, 2018). We identified a long intergenic non-coding RNA (lincRNA) that is expressed in proliferating and differentiated, but not in freshly isolated MuSCs (Fig 1A). Using previously published data (Machado *et al*, 2017; van Velthoven *et al*, 2017), we confirmed

that the expression of the lincRNA is similarly absent in quiescent MuSCs *in situ*. The lincRNA is located in the murine Myh3-Myh13 gene cluster (Fig EV1A) and was previously named linc-MYH due to its localization with the myosin heavy chain gene cluster (Sakakibara *et al*, 2014). The expression of linc-MYH during myogenic differentiation of MuSCs parallels the expression of other genes in the Myh3-Myh13 gene cluster, which is already activated before differentiation but further increases in differentiated myotubes (Fig 1A). Murine MuSCs generate two different isoforms of linc-MYH consisting of four or five exons, apparently resulting from alternative transcriptional start sites (Fig EV1B). We also identified a putative linc-MYH ortholog in the human Myh3-Myh13 cluster based on genomic synteny and expression, although no conservation of the primary lncRNA sequence was recognized between mice and humans (Fig EV1C and D). The expression of linc-MYH is strictly confined to skeletal muscle in both mice and humans (Figs 1B and C, and EV1B), which was confirmed by Genotype-Tissue Expression (GTEx) project data (<https://gtexportal.org/home/gene/CTC-297N7.7>). The expression of linc-MYH is not detected in limb buds in early embryonic stages, and there is low expression in hindlimb muscle at late fetal stages and shortly after birth. However, expression increases in skeletal muscle 3 weeks after birth and is strongly expressed in skeletal muscle 8 weeks after birth (Fig 1D).

We did not detect any conserved open reading frame in mouse or human linc-MYH, suggesting that the linc-MYH is a *bona fide* non-coding RNA. To confirm this assumption, we tested the coding potential of linc-MYH using established tools, including the coding potential calculator CPC (Kong *et al*, 2007) and its updated version CPC2 (Kang *et al*, 2017), which corroborated the low coding potential for both linc-MYH variants (Fig EV1E). The CPC2 tool also revealed a low Fickett score, further confirming that linc-MYH does not code for a peptide (Fickett, 1982) (Fig EV1F). Since we were primarily interested in nuclear lncRNAs, we determined the subcellular localization of linc-MYH. Subcellular fractionation of C2C12 myocytes revealed that linc-MYH is predominantly positioned in the nucleus (Fig 1E). The nuclear localization of linc-MYH was confirmed by RNA-FISH experiments using probes targeting Xist and Adipor RNA as controls (Fig 1F–H). Linc-MYH was detected at multiple locations in the nucleus, suggesting potential functions of linc-MYH outside the myosin cluster, unlike Xist, which is confined to the X chromosome.

Linc-MYH interacts with the INO80 chromatin remodeler complex

To identify putative epigenetic regulators or transcription factors that might interact with linc-MYH, we performed RNA-protein pull-down experiments using nuclear protein extracts from C2C12 skeletal muscle cells. Interacting proteins were isolated using immobilized, *in vitro* transcribed linc-MYH RNA, and subsequently identified by mass spectrometry. Three different control RNA probes were used to distinguish between molecules that promiscuously bind to RNA and proteins that interact specifically with linc-MYH. Analysis of mass spectrometry data by unbiased GO enrichment analysis revealed a striking enrichment of GO terms related to chromatin remodeling complexes (Fig 1I). Only the linc-MYH RNA probe but not the different control RNA probes pulled down several

Figure 1. linc-MYH is located in nuclei of proliferating and differentiated myocytes and interacts with the chromatin remodeler complex INO80.

- A RNA-seq. of freshly isolated, proliferating, and differentiating satellite cells reveals an increased expression of linc-MYH in proliferating and differentiating MuSCs, but no expression is found in freshly isolated MuSCs.
- B, C Expression of linc-MYH is confined to skeletal muscle in mouse (B) and human (C) tissues.
- D Expression of linc-MYH is not detected in limb buds at E10.5 ($n = 3$), E13.5 ($n = 3$), and E15.5 ($n = 3$). Expression of linc-MYH in hindlimb muscle of E18.5, newborn, and 7-day-old animals ($n = 3/3/3$). Expression of linc-MYH in m. soleus (soleus), m. tibialis anterior (TA), and m. extensor digitorum longus (EDL) muscle at 3 weeks ($n = 3$) and 8 weeks of age ($n = 5$). Biological replicates were used for all PCR experiments, and data are mean \pm SEM.
- E-H Murine linc-Myh is localized in nuclear extracts of C2C12 cells. Xist (nuclear) and Gapdh (mainly cytoplasmic) were used as controls ($n = 2$ nuclear/3 cytoplasmic biological replicates.) Data are mean \pm SEM. (F-H) RNA-FISH identifies linc-Myh in nuclei (DAPI, blue) of C2C12 myoblasts. (G) Adipor (cytoplasmic) and (H) Xist (nuclear) were used as controls.
- I, J GO enrichment (I) analysis of proteins pulled down by *in vitro* transcribed RNA from nuclear extracts of C2C12 myoblasts. Linc-MYH RNA and three control RNAs were used in duplicate. (J) Heat map of proteins pulled down in the same experiments as in I, demonstrating that INO80 chromatin remodeler complex exclusively interacts with linc-MYH. Blue color indicates pull-down of the respective protein, and white color indicates that the protein was not detected in the respective sample.
- K, L RNA-IP experiments using an anti-INO80 antibody to isolate the INO80 complex from murine C2C12 cells (K) and human HSMM cells (L). INO80 and INO80 II in L refer to replicate INO80 precipitation experiments. Precipitated RNAs were detected by RT-PCR.

components of the chromatin remodeler INO80 complex, while all RNA probes pulled down prototypical RNA-binding proteins like hnRNPs (Fig 1J).

To validate the interaction between INO80 and linc-MYH in cells, we performed RNA immunoprecipitation (RNA-IP) experiments using an anti-INO80 antibody and extracts from mouse C2C12 myotubes. In the precipitates, RT-PCR analysis detected the mouse linc-MYH, whereas the two different control lncRNAs were not detected (Fig 1K). Similar RNA-IP experiments using human myoblast-derived myocytes (HSMM cells) confirmed our assumption that the putative human linc-MYH ortholog interacts specifically with the human INO80 complex (Fig 1L).

linc-MYH restricts the size of the MuSC pool and prevents hypertrophy of skeletal muscle fibers

We next wanted to understand whether linc-MYH is important for MuSC function and skeletal muscle physiology *in vivo* and therefore generated linc-MYH knockout mice (Appendix Fig S1A–C). Homozygous linc-MYH knockouts were viable and did not display any gross abnormalities. Importantly, however, we observed a substantial increase in the mass of skeletal muscles in mutant animals that correlated with increased body weight compared with wild-type controls (Fig 2A–D). The higher skeletal muscle weight in linc-MYH mutants was also associated with an increase in myofiber cross-sectional area, indicative for myofiber hypertrophy (Fig 2E–J). Furthermore, we detected a strong increase in myonuclei in muscle cross sections (Fig 2K) and in isolated myofibers (Fig 2L–N), suggesting that skeletal muscle hypertrophy in linc-MYH mutants is driven by enhanced generation of MuSCs that fuse to myofibers.

Initiation of linc-MYH expression in MuSCs occurs concomitant to the activation of the Myh3-Myh13 gene cluster and is therefore limited to proliferating MuSCs and differentiated myotubes. Hence, we were surprised to observe a massive increase in Pax7-positive MuSCs attached to isolated myofibers (Fig 2L, M and O) and of Pax7-positive MuSCs on cross sections of tibialis anterior (TA) muscles (Fig 2P–R). The enlarged MuSC pool in linc-MYH-deficient muscles did not show a major change in the activation state under baseline conditions as indicated by the expression of the CalcR (calcitonin receptor), a marker for quiescent MuSCs (Yamaguchi *et al*, 2015; Fig 2P, Q and S). Since activation of MuSCs goes along with reduction in heterochromatin content in MuSCs, we also performed

electron microscopy (EM) on skeletal muscle sections of linc-MYH KO and WT mice. No reduction in heterochromatin was visible in linc-MYH MuSC nuclei (Fig 2U and V), indicating that the increased number of MuSCs is not caused by a loss of quiescence of MuSCs in linc-MYH animals. Nevertheless, we observed a small, but significantly increased number of Pax7⁺/MyoD⁺ nuclei in TA muscle of linc-MYH KO compared with wild-type controls (linc-MYH KO: $8.28 \pm 0.58\%$ of all Pax7⁺ cells, WT: $5.93 \pm 0.6\%$, $n = 3/3$ animals, Mann-Whitney test, one-tailed $P = 0.05$), indicating an increased number of spontaneously activated MuSCs in linc-MYH-deficient muscle. Consistent with increased numbers of MuSCs in TA muscles, we observed higher MuSC numbers in preparations of whole body skeletal muscle of linc-MYH-deficient mice in experiments to isolate MuSCs by FACS (Fig 2T). In line with lower expression of linc-MYH in soleus muscle weight of soleus muscle and cross-sectional area of myofibers was unchanged, but we observe increased numbers of myonuclei and of MuSCs (Appendix Fig S2). In eight-month-old animals, we observe increased number of both myonuclei and of MuSCs as well as increased myofiber cross-sectional area, indicating hypertrophy of the myofibers. Body weight and weight of TA muscle were not significantly increased in 8-week-old animals (Appendix Fig S3).

Control of MuSC proliferation by linc-MYH depends on INO80

To corroborate the molecular interaction between linc-MYH and INO80, we performed an RNA *in situ* hybridization-proximity ligation assay (riSH-PLA; Roussis *et al*, 2017). Since the available INO80 antibodies worked well for immunoprecipitation but not for immunofluorescence, we generated a new mouse strain by insertion of a V5 tag at the C-terminus of INO80 using CRISPR-CAS9-targeted homology-directed repair (Appendix Fig S1D). The resulting INO80-V5 mice were crossed to linc-MYH^{-/-} mutants to generate linc-MYH^{+/+}/INO80-V5 and linc-MYH^{-/-}/INO80-V5 animals from which MuSCs for riSH-PLA were isolated. We detected signals, indicating close proximity of linc-MYH and INO80 in WT myoblasts using biotinylated linc-MYH-specific probes and an anti-V5 antibody (Fig 3A–D), which is in line with the linc-MYH/INO80 co-IP and pull-down results. The interaction of linc-MYH with components of the INO80 complex suggested that linc-MYH might exert its function for limiting MuSC numbers via INO80. To investigate this hypothesis, we generated muscle-specific INO80 mutants using the Pax7-Cre

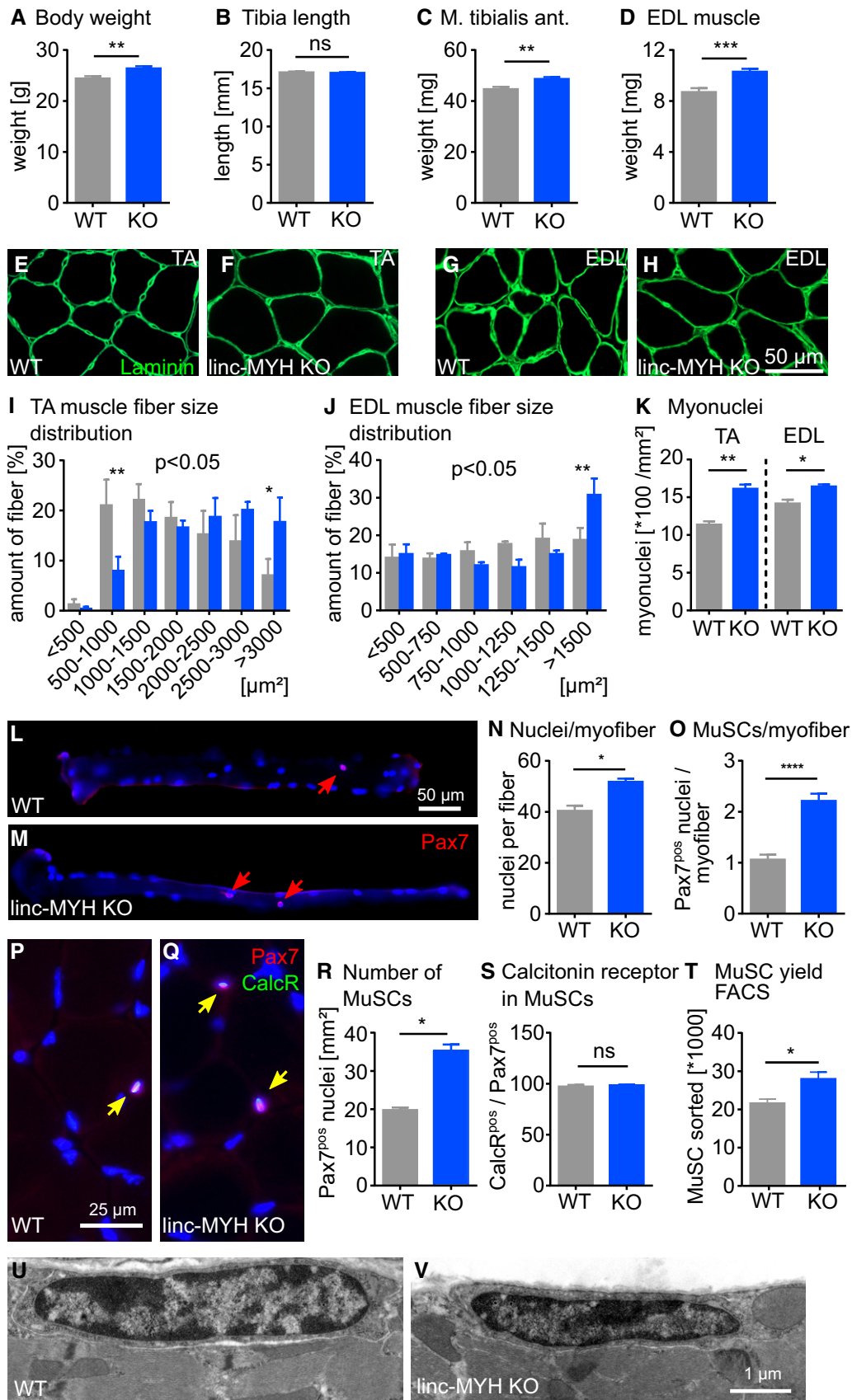


Figure 2.

Figure 2. linc-MYH keeps the number of MuSCs in check and limits muscle fiber growth.

- A, B Body weight (A) of male linc-MYH KO and ctrl mice at 10 weeks ($n = 24$ KO/17 WT; Student's *t*-test, two-tailed, $**P < 0.01$) and tibia length (B) of male linc-MYH KO and ctrl mice of 10 weeks ($n = 9$ KO/13 WT; Student's *t*-test, two-tailed, not significant). Data are mean \pm SEM.
- C, D Weight of m. tibialis anterior (TA) and m. digitorum longus (EDL) of male linc-MYH KO and ctrl mice at 10 weeks ($n = 9$ KO/10 WT for TA, $n = 10$ KO/11 WT for EDL; Student's *t*-test, two-tailed, $**P < 0.01$, $***P < 0.001$). Data are mean \pm SEM.
- E–J Size distribution of fibers in cross sections of TA (E, F) and EDL (G, H) muscle in male linc-MYH KO (blue) and ctrl (gray) animals at 10 weeks. A significant increase in fiber size was observed for TA and EDL muscles of linc-MYH KO mice ($n = 5$ KO/4 WT for TA, $n = 3$ KO/3 WT for EDL muscle, two-way ANOVA with Fisher's multiple comparisons; $*P < 0.05$, $**P < 0.01$; > 250 fibers per animal were counted). Data are mean \pm SEM.
- K Numbers of myonuclei in cross sections of TA and EDL muscle (TA: $n = 6$ KO/6 WT, EDL $n = 3$ KO/3 WT animals, Mann–Whitney test one-tailed, $**P < 0.01$, $*P = 0.05$). Data are mean \pm SEM.
- L–O Number of myonuclei/fiber and of Pax7^{pos} (red) MuSCs (red arrows) on myofibers isolated from flexor digitorum brevis muscle. Nuclei were stained using DAPI (blue). Scale bar in L indicates 50 μ m for L and M. (N) The number of myonuclei/isolated fiber is increased in linc-MYH KO compared with WT myofibers ($n = 4$ KO/4 WT, > 26 fibers/animal; Mann–Whitney test two-tailed, $*P < 0.05$). (O) Number of MuSCs on isolated fibers from linc-MYH KO and WT mice ($n = 4$ KO/4 WT animals, Mann–Whitney test two-tailed, $****P < 0.0001$). Data are mean \pm SEM.
- P–S Number of Pax7 (red)-positive MuSCs in cross sections of tibialis anterior muscle (P–R); the relative amount of quiescent MuSCs identified by double staining (yellow arrows) for Pax7 and Calcr (green) does not significantly differ between WT and linc-MYH KO animals (S). Nuclei were stained with DAPI (blue). Scale bar in P indicates 25 μ m for P and Q. ($n = 3$ KO/3 WT animals, Mann–Whitney test one-tailed; $*P = 0.05$, ns: not significant). All data are mean \pm SEM.
- T The number of MuSC-related events in FACS experiments is significantly increased in linc-MYH-KO animals ($n = 7$ KO/7 WT, Student's *t*-test, two-tailed, $*P = 0.0126$). Data are mean \pm SEM.
- U, V Structure of MuSCs and the heterochromatin content of MuSC nuclei is not changed in linc-MYH KO (V) compared with WT mice (U).

allele (Keller *et al*, 2004) in combination with a floxed Ino80 allele (Qiu *et al*, 2016). Germline mutants of INO80 cannot be used for this purpose, because they are embryonic lethal at early stages of development (Qiu *et al*, 2016). Pax7-Cre^{pos}/INO80^{-/-} mice were viable and did not show any apparent developmental abnormalities including regular numbers of Pax7^{pos} MuSCs (Fig 3E–J), which allowed us to generate linc-MYH^{-/-}/INO80^{-/-}/Pax7-Cre^{pos} double-mutant mice (Pax7-Cre^{pos} dKO). In addition, we used the tamoxifen-inducible Pax7-CreERT2 allele together with linc-MYH^{-/-}/INO80^{-/-} mice to avoid interferences from potentially undetected developmental defects (Murphy *et al*, 2011). Histological analysis of Pax7-Cre^{pos} dKO skeletal muscles revealed a complete abrogation of the increased number of Pax7^{pos} MuSCs observed in linc-MYH^{-/-} mutants (Fig 3E–J), indicating that linc-MYH suppresses an activity of the INO80 complex that is instrumental to enlarge the MuSC pool. Identical results were obtained after inactivation of the *Ino80* gene in adult mice after tamoxifen injection, essentially excluding paracrine, non-cell autonomous functions of the linc-MYH/INO80 complex in adult MuSCs. Furthermore, and in line with the normalization of MuSC numbers, deletion of INO80 in skeletal muscle of linc-MYH^{-/-}/Pax7-Cre^{pos} mice abolished the increased TA muscle weight observed after deletion of linc-MYH (Pax7-Cre^{pos}/INO80^{-/-}: 34.5 mg \pm 0.7 mg, $n = 12$ animals; Pax7-Cre dKO: 33.1 \pm 0.8 mg, $n = 9$ animals). Likewise, the increased bodyweight of linc-MYH animals was normalized by additional deletion of INO80 (Pax7-Cre^{pos}/INO80^{-/-}: 19.5 \pm 0.3 g, $n = 12$ animals; Pax7-Cre dKO: 18.5 \pm 0.8 g, $n = 9$ animals).

To obtain further insights into the cellular processes resulting in increased number of MuSCs after inactivation of linc-MYH, we administered EdU daily over a two-week period to adult animals. WT animals showed incorporation of EdU into approximately 12% of MuSCs confirming previous studies (Pawlikowski *et al*, 2015). More importantly, we observed a great increase in EdU^{pos}/Pax7^{pos} MuSCs in linc-MYH KO mice (Fig 3E–I and K), indicating that more MuSCs were generated by cell proliferation in a fixed time period; however after proliferation, these MuSCs return to a quiescent, Calcr-positive state. In other words, the data suggest that the absence of linc-MYH enhances proliferation of MuSC-derived

myoblasts, which eventually increases the number of quiescent MuSCs. Strikingly, inactivation of INO80 in linc-MYH^{-/-} MuSCs completely abrogated the increase in EdU-labeled quiescent MuSCs (Fig 3E–I and K) and prevented both muscle hypertrophy and the increase of myonuclei numbers in fibers (Fig 3L). Taken together, the data unequivocally demonstrate the critical role of the linc-MYH/INO80 complex in limiting the size of the quiescent MuSC pool, restricting expansion of muscle progenitor cells, as well as highlight the dependency of linc-MYH functions on INO80. In line with increased proliferation, we noted an increased number of MyoD^{pos}/EdU^{pos} nuclei in TA muscle of linc-MYH KO mice (linc-MYH: 5.9 \pm 1.42 nuclei/mm², WT: 2.5 \pm 0.70 nuclei/mm²; $n = 3/3$ animals, Mann–Whitney test, one-tailed $P = 0.05$). The number of MyoD^{pos}/EdU^{pos} nuclei exceeds the total number of Pax7^{pos}/MyoD^{pos} nuclei in linc-MYH and WT control mice (linc-MYH: 2.0 \pm 0.04 nuclei/mm², WT: 0.9 \pm 0.02 nuclei/mm²; $n = 3/3$), suggesting that the majority of MyoD^{pos}/EdU^{pos} nuclei are myoblasts or nuclei of myoblasts recently fused to myofibers and contribute to myofiber hypertrophy.

While the majority of MuSCs are in a quiescent state in adult muscles during steady-state conditions, muscle injury induces activation and proliferation of MuSCs, followed by differentiation and functional replacement of damaged tissue. To analyze whether the increase in MuSCs in linc-MYH mice improves regeneration, we damaged the TA muscle by CTX injections. Surprisingly, we did not detect any differences in the extent of muscle regeneration between WT and linc-MYH mice based on histological assessments, neither at one nor at 2 weeks after damage (Fig EV2A, B and D–I). Interestingly, 4 weeks after CTX injection, when muscle regeneration was completed, we observed the same increase in MuSC numbers in linc-MYH mutant TA muscles compared with WT controls (Fig EV2J–L) and the same increase in EdU-incorporating MuSCs as before the damage (Fig EV2M). The size of myofibers again was increased in regenerated muscles of linc-MYH mutant animals compared with controls, suggesting that inhibition of linc-MYH stimulates MuSC proliferation and skeletal muscle growth during regeneration (Fig EV2C). Additional deletion of INO80 in Pax7-Cre^{pos}/Ino80^{-/-} as well as in Pax7-Cre^{pos}/linc-MYH^{-/-}/Ino80^{-/-}

dKO eliminated the general myofiber hypertrophy observed 4 weeks after CTX-induced muscle damage, and also obliterated the tremendous myofiber hypertrophy observed after loss of linc-MYH (Fig EV2N). More importantly, additional deletion of INO80 resulted in WT levels of both MuSC and of EdU^{pos}/PAX7^{pos} MuSC numbers 4 weeks after CTX-induced damage in INO80 KO and in linc-MYH/INO80 dKO (Fig EV2O and P), abrogating the increase observed in

linc-MYH-deficient muscle. Together, our results indicate that linc-MYH controls proliferation of MuSCs in adult muscle. In line with absent or low expression of linc-MYH in embryonic and juvenile stages (Fig 1D), we detected no increase in the number of myonuclei, of MuSCs, and of EdU-incorporating MuSCs in linc-MYH-deficient muscle at 3 weeks of age (Fig EV3A–E), corroborating the view that linc-MYH controls proliferation of adult MuSCs.

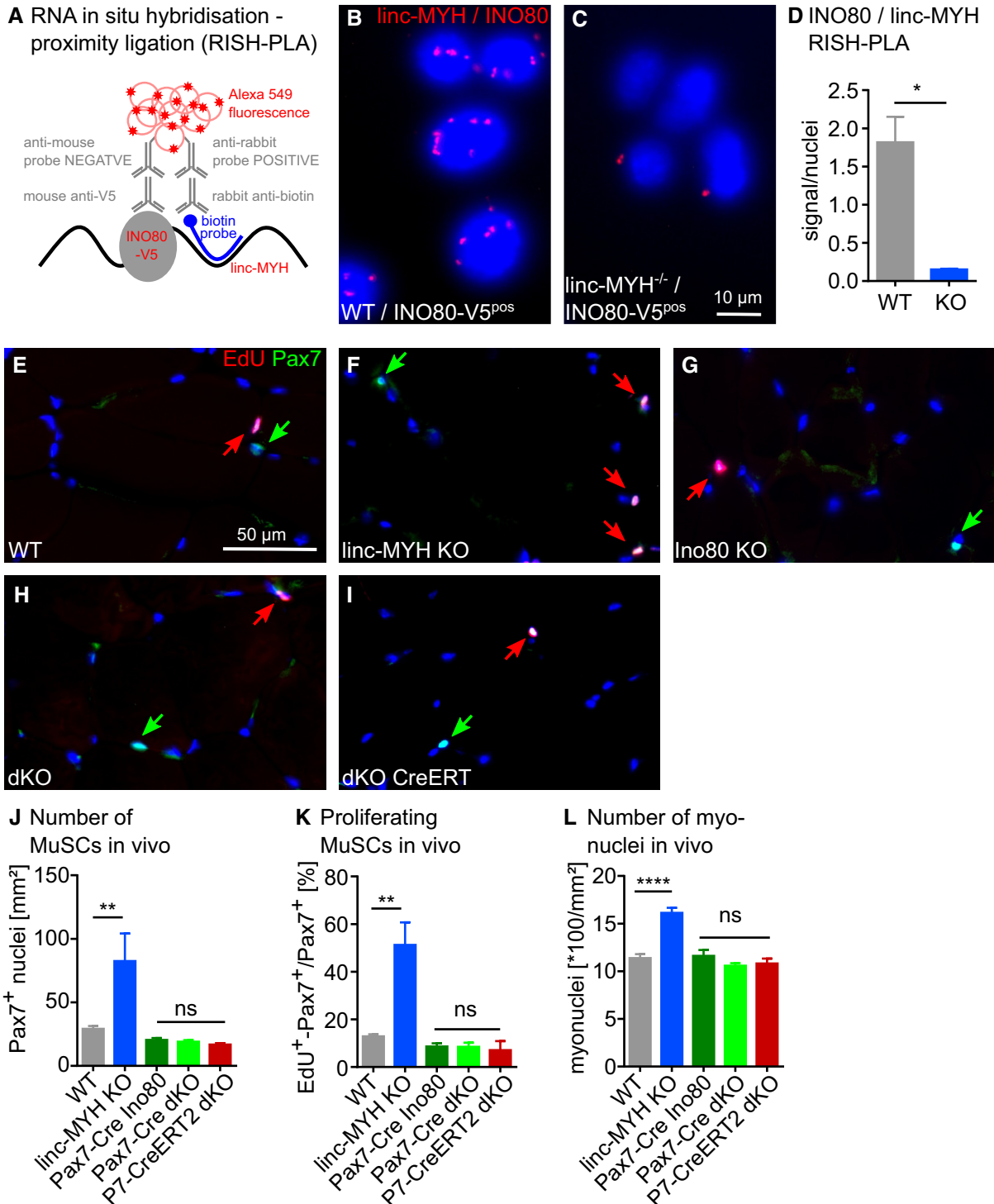


Figure 3.

Figure 3. *linc-Myh* restricts proliferation of MuSCs in an INO80-dependent manner.

- A–D RNA *in situ* hybridization-proximity ligation assay (rISH-PLA) detects the close proximity of a specific RNA with proteins *in situ* modified from Roussis *et al* (B, C) rISH-PLA confirms the proximity of *linc-MYH* to endogenous INO80-V5 in the nucleus of proliferating WT MuSCs (B). The specific signal is lost in *linc-MYH*-deficient MuSCs (C). ($n = 3$ WT/3 KO biological replicates; Mann–Whitney test, $*P = 0.05$). Data are mean \pm SEM.
- E–I Representative images of TA muscle sections of 10-week-old mice stained for PAX7 (green) and EdU incorporation (red). MuSCs without (green arrows) and with EdU-labeling (red arrows) are indicated. (E, F) Deletion of *linc-MYH* results in increased numbers of muscle stem cells and pronounced increase in the ratio of EdU-positive MuSCs. (G–I) The increase in both the number of MuSCs and EdU-positive MuSCs in *linc-MYH* mutant muscle is abolished by constitutive (G: Pax7-Cre^{pos}/INO80^{-/-}, Ino80 KO; H: *linc-MYH*^{-/-}/Pax7-Cre^{pos}/INO80^{-/-}, dKO) and induced (I: *linc-MYH*^{-/-}/Pax7-CreERT2^{pos}/INO80^{-/-}, dKO CreERT) deletion of INO80 in Pax7 expressing cells.
- J–L Statistical evaluation of the number of muscle stem cells observed in TA muscles (J). Statistical evaluation of the ratio of EdU-incorporating MuSCs relative to all Pax7-positive MuSCs (K). Statistical evaluation of the number of myonuclei in myofibers of TA muscles from different genotypes (L); ($n = 5$ WT/5 *linc-MYH* KO/4 Ino80 KO/5 dKO/3 CreERT dKO animals in J/K, $n = 6$ WT/6 *linc-MYH* KO/5 Ino80 KO/6 dKO/3 CreERT dKO animals in L $**P < 0.01$, $****P < 0.0001$, > 31 MSCs/animal in K; ANOVA test with multiple comparisons against WT. Sidak–Holm correction was used. Data are mean \pm SEM).

In contrast to previous shRNA knock-down experiments, claiming a role of *linc-MYH* in muscle fiber type specification (Sakakibara *et al*, 2014), we did not observe any changes in fiber type composition in *linc-MYH*^{-/-}, Ino80^{-/-}/Pax7-Cre^{pos}, or in Pax7-Cre dKO mice (Appendix Fig S4). Moreover, the expression of the respective transcripts was not altered (Appendix Table S1). To exclude any potential effects of the *linc-MYH*^{-/-} allele on the *Myh3-Myh13* gene locus, we generated an additional *linc-MYH*-mutant mouse strain. Using a CAS9/HDR approach, we inserted a poly-A cassette into the first exon of the *linc-MYH* gene which is used by both isoforms (Appendix Fig S1E and F). Insertion of the poly-A cassette prevented *linc-MYH* expression completely (Appendix Fig S1G). Analysis of the *linc-MYH* poly-A-insertion allele revealed an identical phenotype to the deletion allele with no alterations in fiber type composition (Appendix Fig S4) and an increased number of Pax7-positive quiescent MuSCs (Appendix Fig S1H).

To analyze the role of the *linc-MYH*/INO80 complex in the proliferation of MuSCs *in vitro*, we isolated MuSCs from skeletal muscle tissue of WT, *linc-MYH*^{-/-}, Pax7-Cre^{pos}/INO80^{-/-}, and Pax7-Cre dKO mice. Consistent with the *in vivo* data, MuSCs isolated from *linc-MYH*^{-/-} skeletal muscle showed increased proliferation rates, reached confluence much faster compared to WT controls (Fig 4A–F), and displayed increased EdU incorporation. In the early phase of MuSC culture (120 h postisolation) that is characterized by a surge of proliferation of MuSCs, we noticed only a slight increase in EdU incorporation in *linc-MYH*-deficient MuSCs compared with WT MuSCs (Appendix Fig S5A–E). However, 240 h and 315 h after isolation we observed higher EdU incorporation in *linc-MYH* KO MuSCs compared with WT MuSCs (Appendix Fig S5F–O). Deletion of INO80 in contrast to the *in vivo* situation resulted in reduced proliferation of INO80-deficient MuSCs *in vitro*; however in this setting, deletion of INO80 in *linc-MYH*^{-/-} cells fully prevented increased proliferation rates and earlier confluence due to the absence of *linc-MYH* (Fig 4A–F).

Transcriptome analysis reveals enrichment of YY1 and p53 target genes in *linc-MYH*^{-/-} MuSCs

Our results so far clearly indicated that *linc-MYH* exerts its effects via the INO80 chromatin remodeler complex. Hence, we reasoned that analysis of transcriptional changes in *linc-MYH*^{-/-}, Pax7-Cre^{pos}/INO80^{-/-}, and Pax7-Cre dKO MuSCs might provide hints about the underlying regulatory mechanisms. Comparison of *linc-MYH*^{-/-} with WT MuSCs revealed enrichment of GO terms associated with cell proliferation as expected (Fig 4G and J). Importantly,

we also detected a strong enrichment of genes containing binding sites for YY1 and p53, suggesting that some effects of *linc-MYH* on INO80 might depend on YY1 and/or p53 (Fig 4H, K, I, and L). Despite increased expression of genes containing YY1-binding sites, the expression of YY1 or other components of the INO80 complex was not altered at both mRNA and protein levels, indicating that *linc-MYH* might control association of YY1 with the INO80 complex at the post-translational level (Appendix Table S2, Appendix Fig S6). Accordingly, comparison of proliferating Pax7-Cre^{pos}/INO80^{-/-} and Pax7-Cre dKO MuSCs revealed abrogated enrichment of gene sets related to proliferation and enrichment of YY1 and p53 target genes (Fig 4G–L). Additionally, shRNA-mediated knock-down of YY1 in proliferating MuSCs resulted in loss of the increased proliferation observed following deletion of *linc-MYH* (Fig EV4), confirming a role of YY1 in *linc-MYH*/INO80-mediated function in the control of MuSC proliferation.

Furthermore, we detected a strong attenuation of gene set enrichment in Pax7-Cre^{pos}/INO80^{-/-} and Pax7-Cre dKO MuSCs but not in *linc-MYH*^{-/-} MuSCs for DNA strand elongation, telomere maintenance, and chromosome maintenance (Appendix Table S3). This observation fits to the well-documented function of INO80 in genome maintenance and repair (Min *et al*, 2013; Cao *et al*, 2015; Lee *et al*, 2017). In line with these results, we observed increased γ H2AX deposition in nuclei of proliferating Pax7-Cre^{pos}/INO80^{-/-} and Pax7-Cre dKO but not in *linc-MYH*^{-/-} and WT MuSCs (Fig 5A–G). These findings are in line with the results of the respective gene set enrichment analysis data (Fig 5H–I). We therefore concluded that *linc-MYH* specifically controls the function of INO80 in the regulation of MuSC abundance and proliferation but not in DNA repair. The data also suggest that the *linc-MYH*-dependent function of INO80 might rely on YY1, which is a known interactor of the INO80 complex (Cai *et al*, 2007; Wu *et al*, 2007; Chen *et al*, 2011; Runge *et al*, 2018).

The presence of *linc-MYH* changes composition of the INO80 complex

To directly test the hypothesis that *linc-MYH* regulates MuSCs abundance by ruling the composition of the INO80 complex and controlling association of INO80 with YY1 in a cell stage-dependent manner, we performed comparative co-IP experiments in WT and *linc-MYH*^{-/-} skeletal muscle tissues. Immunoprecipitation of INO80 followed by mass spectrometry identified 14 known interaction partners of INO80 including RUVBL1/2, ACTR5, ACTR8, UCHL5, and NFRKB, which were pulled down at comparable amounts both in

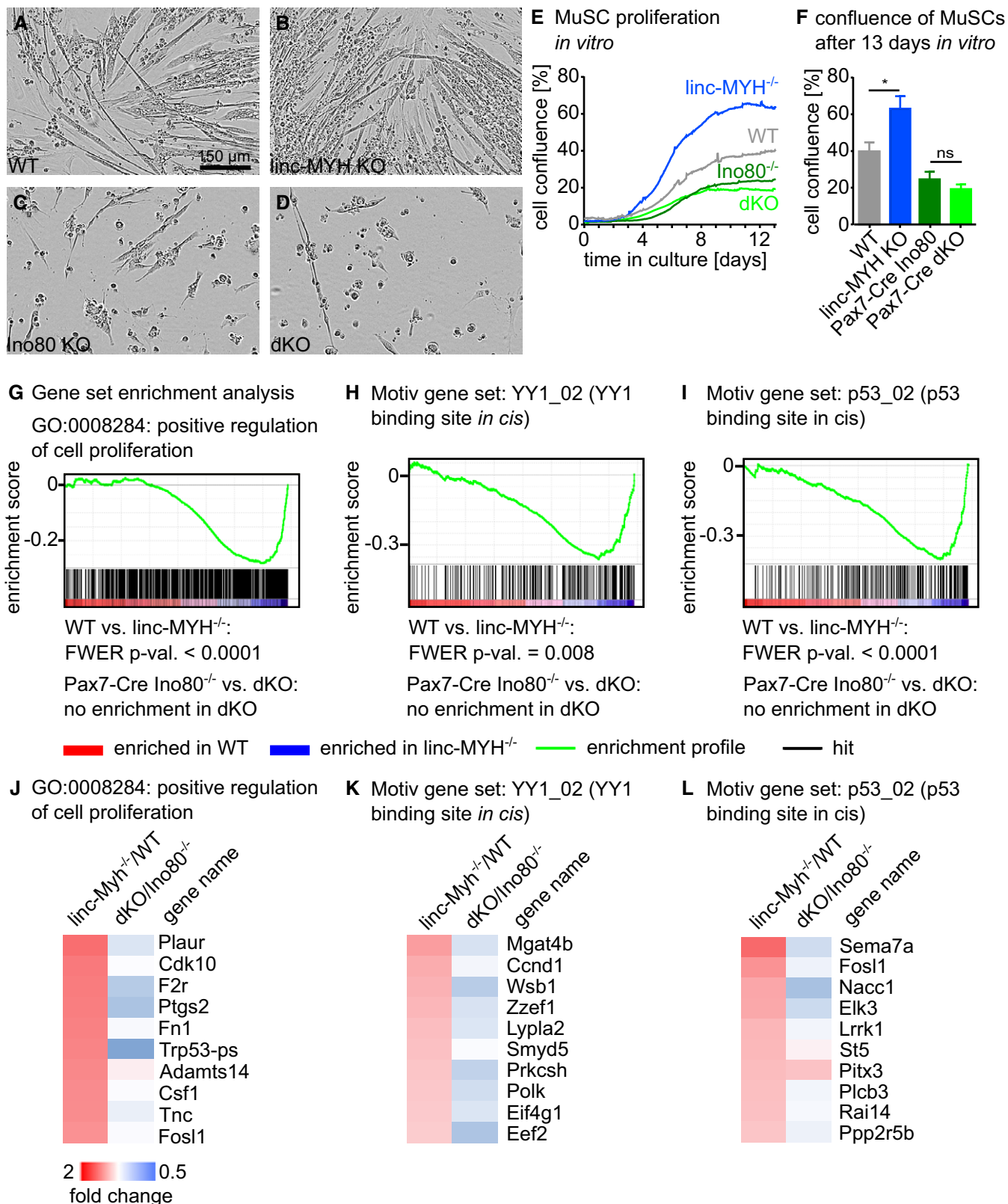


Figure 4.

Figure 4. Deletion of INO80 prevents linc-MYH-dependent changes in MuSC proliferation and gene expression.

- A–D Isolated linc-MYH KO MuSCs reach confluence much faster than WT MuSCs indicating higher proliferation rates. Deletion of INO80 eliminates the difference between Pax7-Cre^{pos}/INO80^{-/-} (Ino80 KO) and linc-MYH^{-/-}/linc-MYH^{-/-}/Pax7-Cre^{pos}/INO80^{-/-} (dKO). Images are representative images for cultures after 13 days in culture.
- E Differences in proliferation rates are abolished by additional deletion of INO80 in MuSCs. Cell confluence was monitored by a live cell imaging analysis system for 13 days ($n = 7$ WT/6 linc-MYH KO/3 Ino80 KO/3 dKO-independent preparations of MuSCs).
- F Statistical analysis of cell confluence after 13 days of muscle stem cell proliferation ($n = 7$ WT/6 linc-MYH KO/3 Ino80 KO/3 dKO-independent preparations of MuSCs, Student's *t*-test, two-tailed; * $P < 0.05$, ns = not significant). Data are mean \pm SEM.
- G–I Gene set enrichment analysis (GSEA, broadinstitute.org) of microarray data from proliferating MuSCs. Comparison of linc-MYH^{-/-} vs. WT proliferating MuSC transcriptomes shows enrichment of genes related to cell proliferation (G), enrichment of genes containing cis regulatory elements for YY1 (H) and p53 (I). Enrichments are highly significant using the most conservative familywise-error rate method (FWER). Enrichments were lost in linc-MYH^{-/-} MuSCs after additional deletion of INO80 (dKOs) compared with Pax7-Cre^{pos}/INO80^{-/-} MuSCs.
- J–L Heat maps of the 10 most upregulated genes of the respective gene sets depicted in G–I in linc-MYH^{-/-} vs. WT MuSCs and in linc-MYH^{-/-}/Pax7-Cre^{pos}/INO80^{-/-} dKO vs. Pax7-Cre^{pos}/INO80^{-/-} MuSCs. The expression of upregulated genes in linc-MYH^{-/-} was normalized after additional deletion of INO80 (dKOs), indicating that effects of linc-MYH completely depend on INO80 (WT $n = 4$, linc-MYH^{-/-} $n = 4$, Pax7-Cre^{pos}/INO80^{-/-} $n = 4$, Pax7-Cre dKO $n = 3$ animals used for independent isolations of MuSCs).

WT and linc-MYH^{-/-} skeletal muscles. Importantly, however, we detected increased amounts of YY1, WDR5, and TFPT in linc-MYH^{-/-} compared with WT IP samples based on label-free quantitative mass spectrometry (Table 1). Additional pull-down experiments in combination with Western blot analysis confirmed these findings. YY1, WDR5, and TFPT were more abundant in INO80 pull-down samples from linc-MYH^{-/-} compared with WT skeletal muscles, while interaction of RUVBL1 and RUVBL2 with the INO80 complex was not affected by the loss of linc-MYH (Fig 6A and B). No changes in the concentration of RUVBL1/2, YY1, WDR5, or TFPT proteins were found in input samples, confirming our previous observation that mRNA expression levels of these molecules are not affected by the absence of linc-MYH (Appendix Fig S6).

The linc-MYH-dependent switch in INO80 complex formation was further corroborated in proliferating MuSCs using *in situ* proximity ligation assays (PLAs). The PLAs revealed increased interaction of YY1 and WDR5 with INO80-V5 in proliferating linc-MYH^{-/-}/INO80-V5 compared with linc-MYH^{+/+}/INO80-V5 MuSCs, while the interaction between RUVBL2 and INO80 remained unchanged (Fig 6C–K).

In an attempt to gain a better understanding of the interaction between linc-MYH and the INO80 complex, we tested different domains of the human INO80 protein (hINO80) (Fig EV5A and B) for interaction with linc-MYH. Pull-down experiments in combination with Western blot analysis revealed that linc-MYH specifically interacts with hINO80 (Fig EV5B). Overexpression of hINO80 protein domains *in vitro* according to the Conaway Lab (Chen *et al*, 2011) revealed that linc-MYH directly interacts with the N-terminal parts of the hINO80 protein, namely the NTD and HSA domains (Fig EV5B). Accordingly, fragments of the hINO80 protein lacking these domains do not interact with linc-MYH (Fig EV5B). In line with this, we identified interaction of linc-MYH with MCRS1 (Fig EV5C), a protein described to interact with the NTD domain of hINO80 (Chen *et al*, 2011). In contrast to this, we detected no specific interactions of linc-MYH with ACTR5, ACTR8, INO80C, RUVBL1, and RUVBL2, although some of these subunits were formerly pulled down in the context of the INO80 complex. Together with our previous findings, and the knowledge that TFPT and YY1 also bind, respectively, to the NTD and HSA domains (Chen *et al*, 2011), we propose that the interaction between linc-MYH and INO80 exclusively takes part in the NTD and HSA domains of the INO80 protein complex.

To test whether the INO80 complex interacts with specific parts of the linc-MYH sequence, we performed pull-down experiments in combination with mass spectrometry analysis of the native mINO80 protein with different exons sequences linc-MYH. We revealed interaction of INO80 with the last three exons of the linc-MYH variant AK010044, two of which are in common with the AK079404. We detected an interaction of INO80 with the first exon of AK079404. However, we detected no interaction with the first two exons of AK010044 (Fig EV5D). These results were validated by performing pull-down experiments using exon sequences of linc-MYH in combination with the overexpressed hINO80 protein. Our results indicate that exon 4 and 5 sequences of AK010044 strongly interact with the hINO80 protein, whereas exon 1 (AK079404) as well as exons 2 and 3 (AK010044) display weaker interactions with hINO80 (Fig EV5E). No interaction with exon 1 (AK010044) was detected. Collectively, our results reveal that exons 3, 4, and 5 appear to be the sites where the interaction between linc-MYH and INO80 is mainly taking part, although the exact structural basis of the interaction remains to be determined.

These results demonstrate that linc-MYH specifically alters composition of the INO80 complex in MuSCs by interacting with the N-terminal parts of INO80. Moreover, linc-MYH directly interacts with MCRS1, a protein known to interact with the N-terminal domain of INO80. Together these interactions hinder recruitment of other N-terminal-binding subunits (Chen *et al*, 2011), namely the pro-proliferative YY1 transcription factor and TFPT. In contrast, linc-MYH does not affect the stoichiometry of core INO80 complex components such RUVBL1/2 and ACTR5/8, which are essential for nucleosome sliding and of ACTR8, needed for recruitment of the INO80 complex to DNA damage sites marked by γ H2AX.

Discussion

Here, we demonstrated that the evolutionary conserved long non-coding RNA linc-MYH plays a major role in the control of MuSC proliferation by specifically regulating composition and activity of the INO80 complex. After deletion of linc-MYH, we observe an increase in both EdU-incorporating Pax7-positive MuSCs and MyoD/Pax7-positive MuSCs. However, we do not observe a general decline of quiescent MuSCs, but rather the opposite since the absolute numbers of quiescent MuSCs are increased. The data clearly

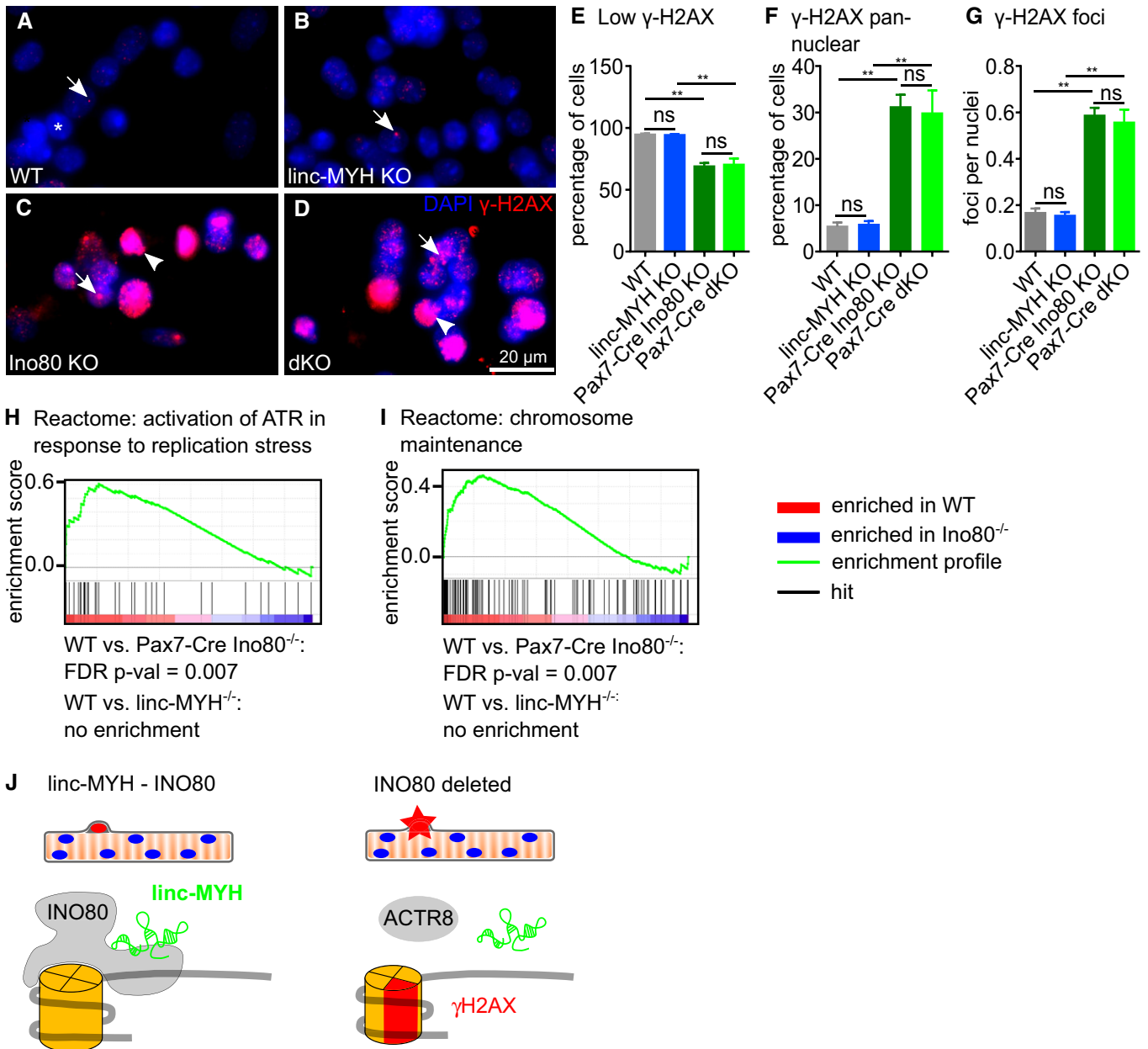


Figure 5. linc-MYH does not regulate the function of INO80 during replication stress.

A–D γ -H2AX staining of proliferating MuSCs from WT (A), linc-MYH-deficient (B), Pax7-Cre^{pos}/INO80 KO (C), and linc-MYH/INO80 dKO (D) mice. Deletion of INO80 results in increased γ -H2AX signals, while deletion of linc-MYH has no effects (asterisk: low γ -H2AX signals, arrow: γ -H2AX-foci detected in nuclei, arrowhead: pan-nuclear γ -H2AX signal).

E–G Statistical evaluation of the presence of γ -H2AX signals in MuSCs of different genotypes ($n = 3/3/3$ animals used for independent isolations of MuSCs, two technical replicates for each animal, and at least 164 cells were counted, Mann–Whitney test, $**P < 0.01$. Data are mean \pm SEM).

H, I Gene set enrichment analysis of microarray data obtained for proliferating MuSCs shows enrichment of genes related to activity of ATR in response to replication stress recovery (H) and enrichment of genes involved in chromosome maintenance (I) in WT compared with Pax7-Cre^{pos} INO80^{-/-} MuSCs. Enrichment of these or similar gene sets was not observed when comparing WT to linc-MYH^{-/-} MuSCs.

J Model of the role of INO80 and linc-MYH in the recognition of γ -H2AX and DNA repair. The DNA repair function of the INO80 complex does not depend on its interaction with linc-MYH.

argue for a function of linc-MYH in proliferating MuSCs, which fits well to the expression profile of the linc-MYH gene that is not transcribed in quiescent and freshly isolated MuSCs but in proliferating muscle stem cells and in myotubes.

linc-MYH is embedded in the Myh3-Myh13 cluster which becomes activated at late stages of proliferation and in differentiating myocytes. Thus, the Myh3-Myh13 cluster seems to provide the regulatory context for linc-MYH expression. Further regulatory cues

Table 1. Identification of linc-MYH-dependent INO80 interaction partners

| Coefficient WT vs. linc-MYH KO | Protein name | Protein description |
|--------------------------------|-----------------------|---|
| -16.17 | TFPT (AMIDA, INO80F) | TCF3 fusion partner homolog |
| -7.49 | KLC2 | Kinesin light chain 2 |
| -7.16 | WDR5 | WD repeat-containing protein 5 |
| -7.01 | YY1 | Transcriptional repressor protein YY1 |
| -6.91 | ACTL6a (ARP4) | Actin-like protein 6A |
| -1.24 | NFRKB (INO80g) | Nuclear factor related to kappa-B-binding protein |
| -0.83 | ACTR8 (ARP8) | Actin-related protein 8 |
| -0.56 | UCHL5 (UCH37) | Ubiquitin carboxyl-terminal hydrolase isozyme L5 |
| -0.53 | INO80 | DNA helicase INO80 |
| -0.19 | RUVBL1 (TIP49a) | RuvB-like 1 |
| -0.17 | RUVBL2 (TIP49b) | RuvB-like 2 |
| -0.17 | ACTR5 (ARP5) | Actin-related protein 5 |
| 7.00 | RAB5c | Ras-related protein Rab-5C |
| 7.44 | HIST2H2AC; HIST2H2AA1 | Histone H2A; type 2-C; type 2-A |
| 7.61 | INO80c (IES6) | INO80 complex subunit C |

Proteins interacting with INO80 in WT and linc-MYH-deficient TA muscle were identified by co-immunoprecipitation in combination with label-free quantitative mass spectrometry. Three independent Co-IP experiments were performed using muscle tissues from WT ($n = 3$) and linc-MYH KO ($n = 3$) animals. A coefficient for relative abundance of individual proteins in WT/linc-MYH KO Co-IP samples was calculated, and results were filtered for known INO80 interacting proteins based on the NCBI record of the human INO80 interactome (<https://www.ncbi.nlm.nih.gov/gene/?term=INO80>). The calculations revealed increased abundance of TFPT, WDR5, and YY1 and reduced abundance of INO80c in INO80 Co-IP experiments. Other core-components of the INO80 complex such as Ruvbl1/2, ACTR5, ACTR8, and NFRKB were unaltered.

specific for linc-MYH might exist (Sakakibara *et al*, 2014), and these result in absent or low expression in embryonic and juvenile muscle and in high expression in adult muscle and differentiating adult MuSCs. From a teleological point of view, such a scenario makes a lot of sense: Cells that are committed to myogenic differentiation and therefore start to activate genes required for sarcomere formation need to turn off proliferation. Co-expression of sarcomere genes and of an anti-proliferative gene such as linc-MYH make sure that both processes are synchronized, reaching a peak in differentiated non-proliferating myotubes, which express the highest levels of Myh genes and linc-MYH. The model might also explain, at least in part, why myogenic cells become refractive to growth factor-dependent stimulation of cell proliferation shortly before differentiation. Apparently, not only paucity of external signals restricts proliferation but also cell autonomous mechanisms that were set in motion to limit expression of pro-proliferative genes (Moore *et al*, 1991; Pawlikowski *et al*, 2017).

The function of linc-MYH for regulation of MuSC proliferation strictly depends on INO80. Several lines of evidence *in vivo* and *in vitro* indicate that without presence of INO80 in MuSCs linc-MYH-deficient MuSCs lose their proliferative advantage and show normalized expression of genes involved in proliferation. We demonstrated that the interaction of linc-MYH with INO80 alters the complex composition, thereby conferring cell stage and cell type-specific functions to this ubiquitously present complex. The core INO80 complex includes over 15 subunits, which serve different functions, and several accessory factors (Chen *et al*, 2011; Tosi *et al*, 2013; Aramayo *et al*, 2018). By preventing recruitment of YY1, linc-MYH targets a specific modality of the INO80 complex, related to the regulation of cell proliferation. YY1 is well known to promote proliferation of myoblasts, MuSCs, and other cells (Wang *et al*, 2017; Chen *et al*, 2019), either by direct transcriptional regulation, or via other mechanisms involving stability of proteins (Chen *et al*, 2019). Although it was already known that several transcriptional effects of YY1 are mediated by interaction with INO80, the regulation of this interaction has been enigmatic (Cai *et al*, 2007). Our experiments reveal that linc-MYH interacts with N-terminal parts of INO80 as well as with the MCRS1 protein also found at the N-terminus of INO80 protein. These interactions obstruct recruitment of N-terminal-binding INO80 extrinsic subunits including TFPT and YY1 (Chen *et al*, 2011). Numerous genes containing YY1 target sites in promoter regions were upregulated in linc-MYH-deficient MuSCs in an INO80-dependent manner, providing clear evidence that linc-MYH prevents access of YY1 to the INO80 complex. YY1 targets include genes known to drive cell proliferation such as *Ccnd1* (Wang *et al*, 2017) and *Eif4g1* (Ramirez-Valle *et al*, 2008; Jaiswal *et al*, 2018). Knock-down of YY1 eliminates the differences in MuSC proliferation between linc-MYH KO and control MuSCs, additionally supporting the notion that the prevention of YY1 interaction with the INO80 complex is an important feature of linc-MYH function.

We also observed upregulation of p53 target genes after deletion of linc-MYH, which might be due to the previously described co-activation of p53 target genes by YY1 (Yakovleva *et al*, 2004). The upregulation of p53 target genes might support MuSC integrity during increased proliferation (Begus-Nahrmann *et al*, 2009; Liu *et al*, 2018) and help myoblasts to return to quiescence (Flamini *et al*, 2018) as it has been described for hematopoietic stem cells (Liu *et al*, 2009). Linc-MYH reduces association of the INO80 complex with WDR5, which might represent a more indirect means to limit proliferation of MuSCs. WDR5 is a known adaptor protein that might connect the INO80 chromatin remodeler to the transcriptional activator MLL. In fact, the interaction of INO80 and WDR5 has been previously described to support cell type-specific transcriptional regulation (Cai *et al*, 2010; Wang *et al*, 2014; Zhou *et al*, 2016). Hence, exclusion of WDR5 from INO80 via linc-MYH might reduce transcription of genes supporting proliferation of MuSCs. It is possible that recruitment of WDR5 to the INO80/YY1 complex specifically enhances transcriptional activity of the pro-proliferative YY1/INO80 complex, although we did not investigate these possibilities. However, we did not detect components of the MLL complex in the INO80 pull-down experiments. Thus, interaction of the WDR5 adapter protein with INO80 might have a different MLL-independent function as previously described in a different context (Dias *et al*, 2014).

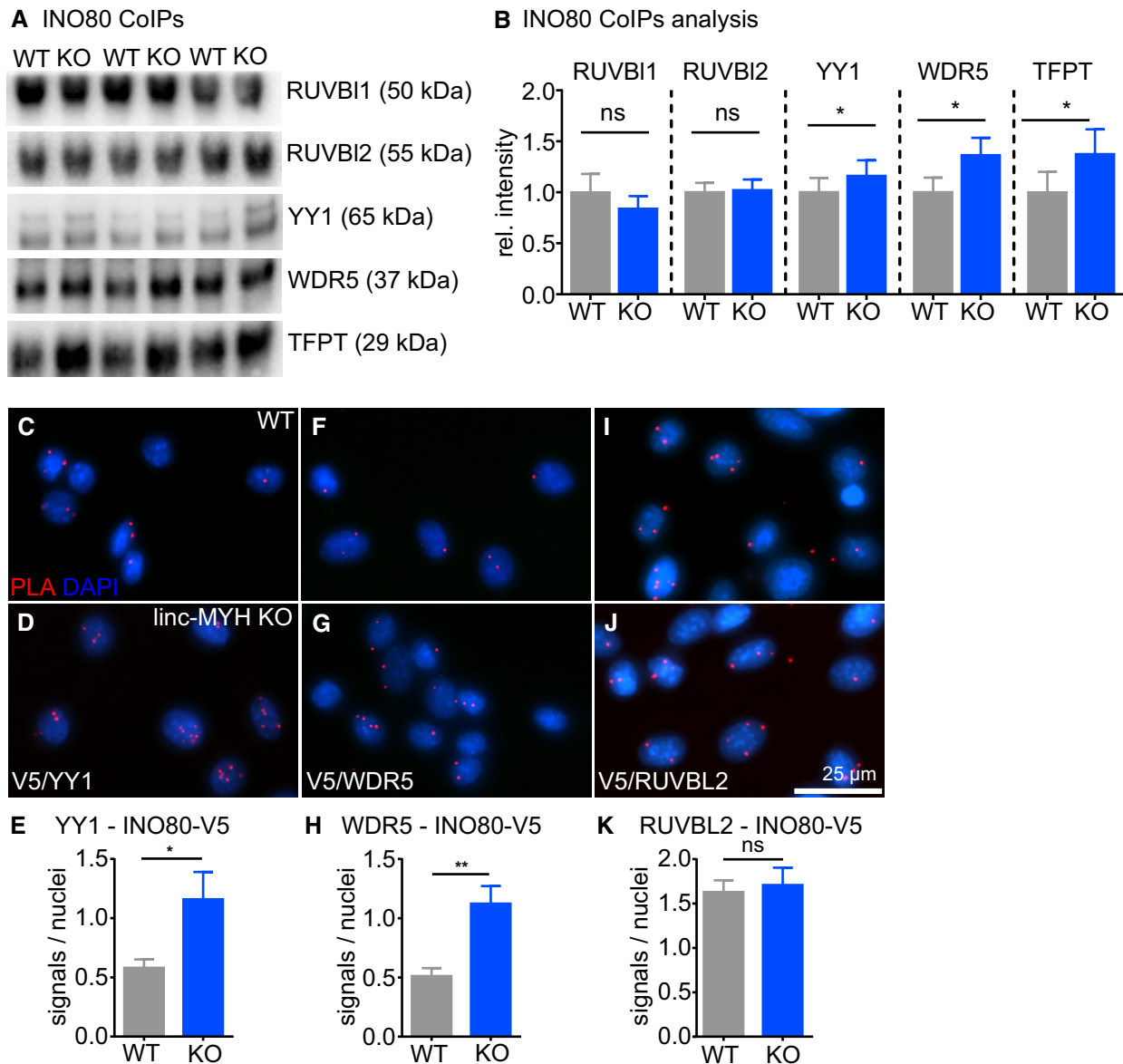


Figure 6. linc-MYH modulates INO80 complex composition by reducing incorporation of YY1 and WDR5.

A, B Co-Immunoprecipitation of INO80 complex subunits from TA muscles of WT and linc-MYH KO mice followed by Western Blot analysis. (B) Statistical analysis of Co-IP/Western Blot data. The amount of RUVBL1 and RUVBL2 in the INO80 complex is not changed after deletion of linc-MYH, while the amounts of YY1, WDR5, and TFPT pulled down by INO80 increase ($n = 3$ WT/3 linc-MYH KO animals; one-way ANOVA, multiple comparisons by Fishers LSD test, $*P < 0.05$). Data are mean \pm SEM.

C–K Proximity ligation assays between INO80 and YY1 (C, D), INO80 and WDR5 (F, G), and INO80 and RuvBL2 (I, J) in proliferating MuSCs. Red signals indicate close proximity of INO80-V5 and the respective interacting protein. Nuclei were stained using DAPI (blue). Statistical evaluation of proximity ligation assays indicating increased interactions of INO80-V5 and YY1 (E, $n = 3/3$ animals, three independent wells per animal, two-tailed students t -test, $*P < 0.05$) and of INO80-V5 to WDR5 (H, $n = 2$ (WT)/2 (KO) animals, three independent wells per animal, two-tailed students t -test, $**P < 0.01$). No increase in proximity was detected between INO80-V5 and Ruvbl2 (K, $n = 2$ (WT)/2 (KO) animals, three independent wells per animal, two-tailed Student's t -test, ns: not significant). Specificity of all analyzed signals was analyzed using single primary or single secondary antibodies in PLA assays. No signals were detected for these controls. Data are mean \pm SEM.

Remarkably, linc-MYH did not affect the stoichiometry of core nucleosome-sliding INO80 complex components such as RUVBL1/2 and ACTR5/8 (Aramayo *et al*, 2018; Brahma *et al*, 2018; Eustermann *et al*, 2018), nor the function of the INO80 complex in DNA repair and recovery from replication stress (Vassileva *et al*, 2014). Packaging of DNA into chromatin is a major obstacle to repair

double-strand breaks and allow base excisions repair. This obstacle can be resolved by modulation of nucleosome structures via chromatin remodelers providing access of signaling and repair machineries to damaged DNA (Morrison, 2017). INO80 seems particularly important in this respect. Several studies demonstrated that the chromatin remodeling and nucleosome-sliding properties of the

INO80 chromatin remodeler are crucial to deal with consequences of DNA damage and replication stress in different organs and mammalian cell types (Ayala *et al*, 2018; Eustermann *et al*, 2018). The ACTR8 subunit is essential for recruitment of the INO80 complex to DNA damage sites marked by γ H2AX, thereby facilitating DNA repair (Kashiwaba *et al*, 2010; Vassileva *et al*, 2014). We found that linc-MYH did not affect the presence of ACTR8 in the INO80 complex, allowing normal replacement of γ H2AX in linc-MYH mutant MuSCs. Accordingly, we only observed attenuated enrichment of gene sets associated with DNA strand replication and telomere maintenance in INO80 and INO80/linc-MYH mutant MuSCs but not in linc-MYH mutant MuSCs. The specific effect of linc-MYH on the pro-proliferative function of the INO80 complex without affecting DNA repair functions is important: Increased expression of pro-proliferation genes and enhanced cell proliferation generates more replication stress, which has to be handled. Molecules acting on complexes regulating both DNA repair and cell proliferation need to avoid reduction in DNA repair activities when regulating proliferation.

The crucial role of linc-MYH in controlling INO80 complex formation and transcriptional activity for regulation of MuSC proliferation also has important consequences for skeletal muscle physiology. We found that the increase in proliferating MuSCs in skeletal muscles of linc-MYH mice resulted in myofiber hypertrophy as indicated by increased cross-sectional areas. Since myofibers in linc-MYH mutant animals contain increased myonuclei contents and show no signs of endomitosis, we reason that muscle hypertrophy is caused by the fusion of supernumerous MuSCs to myofibers (Abmayr & Pavlath, 2012). One might wonder why evolution has shaped a role for linc-MYH to limit skeletal muscle hypertrophy, which is widely assumed to be beneficial. Yet, unnecessarily increased muscle mass boosts energy demand and is an evolutionary liability when food supply is limited. In fact, gene variants causing hypermuscularity, particularly in humans, are relatively rare. A popular example is the myostatin gene, which prevents skeletal muscle hypertrophy (Schuelke *et al*, 2004; Das *et al*, 2019). It has been argued that energy expenses in the skeletal musculature have been traded for enhanced growth of energetically costly brains, essentially postulating reciprocal evolution of brain and muscles (Bozek *et al*, 2014).

Increased proliferation of MuSCs might be beneficial for regeneration of skeletal muscle. Yet, we did not detect signs for enhanced skeletal muscle regeneration in linc-MYH so far, which might in part be due to the CTX damage model, causing severe depletion of MuSCs (Hardy *et al*, 2016). Failure to detect an advantage of linc-MYH-deficient mice in the early stage of muscle regeneration might be explained by the massive stimulation of MuSC proliferation by external cues dominating the control of proliferation of MuSCs early after CTX damage, while linc-MYH rules the control of MuSC proliferation under conditions of muscle homeostasis. This is mirrored in the MuSCs *in vitro*, where the early strong proliferation in response to isolation is not significantly different between WT and linc-MYH-deficient MuSCs, but higher proliferation is observed in linc-MYH-deficient MuSCs at later stages of MuSC proliferation. *In vivo* in later stages, we found exaggerated hypertrophy of individual myofibers after CTX-induced muscle damage, which increased heterogeneity among muscle fibers compared with undamaged muscles from linc-MYH mutants and regenerated muscles of control animals. We did

not analyze effects of a loss of linc-MYH in pathological conditions or during aging, which might generate a different scenario, in particular since aging goes along with a severe decline of MuSC proliferation and a reduction in MuSCs (Garcia-Prat *et al*, 2013). We observed increased MuSC numbers and proliferation in 8-month-old mice, and it would be interesting to investigate whether the increased proliferation rate of linc-MYH KO MuSCs prevents some consequences of skeletal muscle aging and thus might be used for therapeutic purposes.

Much to our surprise and in addition to increased proliferation, we observed a strong increase in quiescent MuSCs in linc-MYH-deficient muscles, although linc-MYH is not expressed in quiescent but only in proliferating MuSCs. The increase in quiescent MuSCs is stable, depends on the presence of INO80 in MuSCs, and is re-established even after extensive muscle damage and subsequent regeneration. The most plausible explanation for this finding is that the extent of MuSC proliferation determines the size of the quiescent MuSC population. Increased numbers of proliferating MuSCs might enhance the chance of stochastic or nonrandom asymmetric cell divisions, required for formation of the stem cell niche (Almada & Wagers, 2016; Feige *et al*, 2018). Such a process has to occur relatively late during MuSC expansion, at a time point when the linc-MYH gene within the Myh3-Myh13 cluster is activated. Nonetheless, we cannot rule out a more indirect mechanism, in which an enlarged population of late-stage proliferating MuSCs signals back to still resting MuSCs, thereby regulating early cell decision events that determine the fate and size of the quiescent MuSC pool.

In summary, we identified a novel mechanism that limits expansion of MuSCs during postnatal skeletal muscle development and regeneration by upregulation of the evolutionary conserved long non-coding RNA linc-MYH. Linc-MYH acts as a selective molecular switch by preventing association of YY1 and WDR5 with the INO80 chromatin remodeler complex. Incorporation of linc-MYH into the INO80 complex eradicates the pro-proliferative capacity of the complex but leaves its DNA repair functions intact. Removal of the linc-MYH-dependent molecular switch enhances proliferation of MuSCs, causes hypertrophy of skeletal muscle fibers, and increases the number of quiescent MuSCs. The linc-MYH example provides a paradigm of how lncRNAs add new layers of regulation to specifically control complex cellular functions in mammalian cells.

Materials and Methods

Animal models

The genomic locus coding for both isoforms of linc-MYH (AK010044 and AK079404) was deleted from the mouse genome by homologous recombination. A 16.7 kb genomic fragment ranging from GCGGCCGCTGTGCTTTCCACCTACCAC to ATAGCGTCCATAGTTC TGGAGGTCC was inserted into a pKO II vector containing a diphtheria toxin selection cassette by Gap-repair (Warming *et al*, 2005) using a BMQ mouse BAC clone (BMQ105-D23; Source BioScience; #BMQ105-D23; Adams *et al*, 2005). An AscI site was inserted into the AvaI digested vector using oligonucleotides, and a loxP-flanked neomycin resistance cassette was inserted using this site. Homologous recombination events in embryonic stem (ES) cells were detected by Southern Blot by a PCR-generated probe

(CGAACAGTGCTTCTCCAAGAAGGT/TATCAGGGAGGAAGTCTTCA GGTC) using *AvaI* digested genomic DNA. Mice were generated from ES cells using standard procedures. The neomycin resistance cassette was removed by FLP recombination using ACTB-FLPe mice (Rodriguez *et al*, 2000) to generate the *linc-MYH*^{KO/(-/-)} allele. Genotypes of mice were determined by PCR using oligonucleotides (AGCTCTGAAACTCCAGAATCTGCCT, CCGCCCTGAGCAGAAT GAATGGACG, CTCGTTGTCAGTTCTGTATAGACCC). The 266-bp fragment identifies the WT allele, and the 417-bp fragment identifies the FLP-deleted allele.

A second *linc-MYH* loss of function model was generated by insertion of a poly-A cassette into the third exon of 2310065F04Rik-201/ENSMUST00000125538.7/AK010044 using CRISPR-CAS9-targeted homology-directed repair. Insertion of the cassette also represses transcription of the variant 2310065F04Rik-202/ENSMUST00000153497.1/AK079404. The guide RNA CAGCTCATT GAACAGTCGAG was inserted into pSpCas9(BB)-2A-Puro (PX459) V2.0 (addgene#62988), and the resulting vector was transfected into ES cells together with the oligonucleotide (ACAAATGAGCCTGGTC AGAGATTGTGAGCCCTGCCTTTGAATCACCTGGGTAGATCTGCA AGTTACTGATAATTCTGTTACAAATAAAGCAATAGCATCACAAA TTTCACAAATAAAGCATTFTTTTCAGGGTCCAAGCTCCAGGCTTTT CCAAAGTTCCTTCCACGGTTGTGATGTGCAGGAAGAAGTCAAAGG CCCT) using the Lipofectamine protocol (Ran *et al*, 2013). ES cells were selected using puromycin (2 mg/ml, 1 day after transfection for 2 days), and recombinant clones were identified by PCR (GTCTTACATTACCTACCTAGAAGGA, GGTTACAAATAAAGCAA TAGCATCA/CCTGTCAGAAACCTCAGATACCATC). PCR fragments of 237-bp indicate the WT allele, while the 259-bp fragment indicates presence of the poly-A allele. Mice were generated from ES cells using standard procedures. Chimeric mice were mated to C57BL/6, and animals used for analysis were backcrossed to C57BL/6 for > 3 generations. For MuSC and muscle-specific deletion of *INO80*, a floxed *Ino80* allele (Qiu *et al*, 2016) and a *Pax7-Cre* driver strain were used (Keller *et al*, 2004). To delete *INO80* in adult MuSCs, the *Pax7-CreERT2* allele (Murphy *et al*, 2011) was used together with tamoxifen injections (75 mg/kg BW for 5 days at 6 weeks of age).

A V5 tag was inserted at the C-terminus of *INO80* using CRISPR-CAS9-targeted homology-directed repair. The guide RNA (gCCTCTGGAGGACGGTAACCA) was inserted into pSpCas9(BB)-2A-Puro (PX459) V2.0 (addgene#62988), and the resulting vector was transfected into ES cells together with the oligonucleotide (CCTAAAAGCCTCCACATGACCAGCAGCCTAGCCTCAGACTCCTTG ATCCGAAACAAGGCAAAGGCACCAACCCCTCGGAGGACGCCCC GTGGTTGTAAGCCTATCCCTAACCTCTCCTCGGTCTCGATTCTA CGTAGTAATAACCATCGTAACCATCTCTGCCCTCTAGCTTCCTTCA ACCAAACCAGGGGCTACA) using the Lipofectamine protocol as above. Recombinant clones were identified by PCR using the oligonucleotides (GTCCGACCTGCTGGCCTTGAG/GCCATCCAAA GACCACCTATGGC). The 266-bp PCR fragment identifies the WT allele and the 332-bp fragment the *Ino80-V5* allele. For FACS isolation of MuSCs, the transgenic *Pax7-ZsGreen* reporter (Bosnakovski *et al*, 2008) was mated to the respective mouse lines.

Mice were kept in IVC with *ad libitum* access to water and food. All animal experiments were done in accordance with national and European community guidelines and were approved by the Committee for Animal Protection of the State of Hessen (Regierungspraesidium Darmstadt).

EdU and Cardiotoxin administration in adult mice

Mice were intraperitoneally injected using 10 µl/g BW labeling solution (5 mg/ml EdU in 0.9% saline; Thermo# E10187) to identify newly synthesized DNA *in vivo*. Adult mice were injected daily for 14 days and 3-week-old animals for 5 days; skeletal muscle tissue was recovered 24 h after the last injection. Cardiotoxin injection into the TA muscle was performed as described previously (Boonsanay *et al*, 2016). Briefly, animals were anesthetized by intraperitoneal injection of Ketamine/Xylazine and one leg of the animal was shaved. The needle of the 0.06 mg/ml cardiotoxin-containing syringe (Sigma#C9759-5MG) was inserted along the center of the TA muscle from foot toward the knee and 50 µl of a 0.06 mg/ml cardiotoxin solution was injected into the TA muscle while retracting the needle. For analgesia, the animals received metamizole via the drinking water (1.6 g/l Novaminsulfon; Zentiva).

RNA-Fluorescence *in situ* hybridization (RNA-FISH)

linc-MYH FISH was done using the ViewRNA ISH cell assay kit from Panomics (#QVC0001) with probe sets detecting *linc-MYH* (VX1-99999-01; Alexa Fluor 546, custom-designed against AK010044), *Xist* (VB4-18068, Alexa Fluor 488), and *Adipor* (VB4-16777, Alexa Fluor 488). Hybridization and detection were performed according to the supplier's instructions with fixation of differentiated C2C12 (ATCC) cells in 1% formaldehyde for 10 min and one hour of trypsin incubation.

RNA-protein pull-down

Proteins interacting with candidate RNA molecules were identified by an *in vitro* RNA-protein pull-down approach in combination with MS analysis. Control lncRNAs were used in addition to *linc-MYH* isoforms to detect unspecific RNA-protein interactions. Templates for RNA synthesis were obtained by PCR amplification using Phusion DNA polymerase (Thermo Scientific, F-553L) based on a plasmid template and primers supplying a T7 promoter sequence (*linc-MYH*, AK079404: Source BioScience#9830118E10, GTAATACGACTACTATAGGGCTCTCTCGGCTCAGCCCTGAGTG TCTCCAGAGG, ATCACAACATCCTTGTGGGGATTATA-TTGC) or by linearization of plasmid templates (AK142388, *Fantom#D430033I02*, *Apal*; MG243346, *Fantom#D430033I02* plus PCR amplified 5' sequence, *Apal*; AK009488: Source BioScience#2310024A14, *BamHI*). Templates for individual exons or parts of exons and templates for controls were amplified using oligonucleotides described in Appendix Table S4. An additional control was prepared using a plasmid template (AK086006, *Fantom#D830044D09*, *BamHI*). RNA was synthesized from templates by the T7 RiboMAX™ Express Large Scale RNA Production System (Promega #P1320) following the manufacturer's instructions, but with transcription time extended to 2 h. 50 pmol of RNA was biotinylated using the Pierce™ RNA 3' End Desthiobiotinylation Kit (Thermo Scientific #20163). Biotinylated RNA was recovered by mini Quick Spin RNA Columns (Roche#11814427001). Nuclear proteins of C2C12 myocytes were isolated using the NE-PER Nuclear Protein Extraction Kit (Thermo#78833). The interaction of *linc-MYH* with human *INO80* was investigated using HEK293 (ATCC) cells overexpressing FLAG-tagged full-length *INO80* or fragments of human *INO80*.

These plasmids were a gift from Joan Conaway (addgene plasmid#: 44149, 29440, 29441, 29443, 29446; Chen *et al*, 2011). In addition, we used extracts of HEK293 cells expressing MCRC1 from a custom gene synthesized vector (Appendix: MCRC1 expression vector; BioCat). The plasmids were transfected using Lipofectamine 3000, and cells were lysed 48 h after transfection in extraction buffer (0.1 M Tris-HCl pH 8.0, 0.01 M EDTA, 10% SDS, Aqua dest, 1× cOmplete Protease Inhibitor cocktail, Roche #4693132001) by sonication. Biotinylated RNA and protein extracts were processed using the Pierce™ Magnetic RNA-Protein Pull-Down Kit (Thermo Scientific #20164) according to the manufacturer's instructions with some modifications (four instead of three washing steps before elution of RNA-bound proteins). In case of C2C12 cell extracts, the eluted proteins were prepared for mass spectrometry analysis by in solution digest. In case of HEK293 cell extracts, the eluted proteins were analyzed by Western blot.

RNA immunoprecipitation (RNA-IP)

RNA immunoprecipitation followed published protocols (Moran *et al*, 2012; Schweisgut *et al*, 2017). 50 µl Dynabeads® Protein A (Thermo Scientific 10001D) was washed twice with 300 µl RIPA Buffer (50 mM Tris-HCl pH 7.4, 1% NP-40, 0.25% sodium-deoxycholate, 150 mM NaCl, 1 mM EDTA) using a magnetic stand for separation of the beads. Beads were incubated with 8 µg of the respective antibody in 500 µl RIPA anti-Ino80 antibody (anti-INO80: Abcam#ab197043 (C2C12 cell IPs) or Abcam#ab118787 (HSMM cell IPs); IgG: Invitrogen#10400C) for 2 h at 4°C on a rotating wheel. C2C12 cells (ATCC #CRL-1772™; DMEM 4.5 g/l Glucose, 10% FCS, 1% Pen/Strep/Glutamine) were grown to confluence, and myotube differentiation was induced for 4–5 days using differentiation medium (DMEM 4.5% Glucose; 2% horse serum, Thermo Scientific #16050130; 1% Pen/Strep/Glutamine). C2C12 cells (six 15-cm plates for one experiment) were trypsinized, washed two times using PBS, and re-suspended at 2×10^6 cells/ml. HSMM (Lonza #CC-2580; six 15-cm plates for one experiment) cells were incubated in SKGM™-2 (Lonza #CC-3245) medium until they reached 80% confluence followed by culture in DMEM-F12 (Thermo Fisher #11320-033). Cell suspensions were incubated with 1% formaldehyde (Thermo #28908) for 10 min at room temperature. Thereafter, glycine was added to a final concentration of 0.125 mM, and cells were washed two times using PBS and re-suspended in 2.4 ml RIPA buffer including cOmplete proteinase inhibitor (Roche# 04693159001) and RNasin 1:100 (Promega# N2615). Cells were lysed using a Covaris Evolution E220 (1 min, 100 W peak power, 200 cycles/burst, 2.0 duty factor), and cell debris was removed by centrifugation (5,000 g, 5 min). 100 µl of the lysate was saved for RNA isolation (input). Antibody-bound beads were washed twice using 400 µl RIPA and incubated over night with 1 ml cell lysate on a rotating wheel at 4°C. After incubation, beads were separated from the supernatant, which was saved for subsequent analysis, and washed 4 times using 500 µl RIPA (4°C). Thereafter, beads were washed 4 times using 500 µl of high-salt RIPA (50 mM Tris-HCl pH 7.4, 1% NP-40, 0.25% sodium-deoxycholate, 150 mM NaCl, 1 mM EDTA, 4 M Urea) and once using PBS. The pellet was re-suspended in 100 µl Buffer C (Tris-HCl 50 mM pH 7.4, NaCl 150 mM, 5 mM EDTA pH 8.0, 10 mM DTT, 1% SDS), 10 µl Proteinase K (Thermo Scientific #EO0491), and 1 µl RNasin (Promega #N2511) was added.

Samples were incubated at 42°C for 30 min, followed by 4-h incubation at 65°C, and 1 ml TRIzol was used for RNA isolation. RNA was further purified using RNAeasy clean-up kit (Qiagen #74104), and RNA was eluted in 30 µl, 8 µl of RNA was used for RT reaction, and PCR was performed using specific oligonucleotides (linc-MYH, AK010044: CTATGTTTTGCCAGTCTCTGCTATG, AACACTATAGC CCTCAAGATGGGAGG; ctrl-lincRNA1, AK07210: GTCTCACCATTCC-TAGGCTGCCAGC, CAAGGCCACTCTGATGGAGGCACT; ctrl-lincRNA2, AK014378: GTCCTGAGCAGTCCAGGCTGGAAGC, CGACA ACTCAGTGCTCAGGAATGTC; hsa-linc-Myh, AK097500: CATGGT CTTGACACTTTGAGGACTA, TTGCATAAATGAGTCCGATGCACAG; hsa-Gapdh: ACCACAGTCCATGCCATCAC, CATGCCAGTGAGCTT CCCGT).

Isolation of myofibers and immunostaining

To isolate myofibers, the *flexor digitorum brevis* muscle was extracted from hind limb feet and digested in 1 ml 0.1% Collagenase P Solution (Sigma-Aldrich #11213873001) in DMEM (Sigma-Aldrich #D5796) for two hours. Fibers were isolated by pipetting the digested muscle up and down with a Pasteur pipette until individual single fibers were visible. The single fibers were transferred to DMEM with 10% FCS (Gibco#10270106) and 1% PSG (Thermo Fisher Scientific #10378016) in a FACS sorting tube (Fisher Scientific #352235). Immunofluorescence staining was performed as described for cryosections, but free floating fibers were collected at the bottom of the staining tube by gravity.

Immunofluorescence stainings

For immunofluorescence staining, 10 µm cryosections mounted on Superfrost Ultra Plus slides (Thermo#J3800AMNZ) were used. Tissue sections were dried at room temperature, fixed for 5 min using 4% paraformaldehyde/PBS, washed three times 10 min using 0.3% Triton X-100/PBS, and incubated in blocking solution (0.01% Triton X-100, 1/10 Blocking One (Nacalai#03953-95)/PBS). When using mouse monoclonal antibodies, Mouse-on-Mouse Blocking Reagent (Vector labs#MKB-2213) was added 1:25 to the blocking solution. After blocking, sections were washed 10 min using PBS and sections were incubated with primary antibodies (mouse anti-PAX7, R&D systems#MAB1675; rabbit anti-Laminin, Sigma#L9393 or rabbit anti-CalcR, Bio-Rad #AHP635, rabbit anti-MyoD, Abcam #ab64159, rabbit anti-γH2AX, Cell Signaling #2577) in solution A (Nacalai Tesque #02272-74) at 4°C overnight. Sections were washed three times 10 min in 0.01% Triton X-100/PBS. Subsequently, sections were incubated with secondary antibodies (goat anti-mouse IgG-Alexa Fluor488, Jackson#115-545-205; goat anti-mouse IgG-Alexa Fluor 594, Jackson#115-585-205; goat anti-rabbit IgG-Alexa 488, Thermo#A11070; goat anti-rabbit IgG-Alexa 680, Thermo#A21076) in solution B (Nacalai Tesque # 02297-64) for 1 h and washed two times using 0.01% Triton X-100/PBS. DAPI (Sigma-Aldrich #10236276001) was applied 1:1,000 in 0.01% Triton X-100/PBS for 5 min, and after a final washing step, sections were embedded in Fluoromount W (Serva #21634.01). Staining for EdU incorporation was done after the three Triton X-100 washing steps according to the supplier's manual. The Click-iT™ Plus EdU Alexa Fluor™ 594 Imaging Kit (Thermo Fisher #C10639) was used for all EdU experiments.

Identification of skeletal muscle fiber types was performed as described previously (Wust *et al*, 2018). Concentrated monoclonal antibodies against 1 MyHC (DSHB #BA-D5), 2A MyHC (DSHB #SC-71), 2B MyHC (DSHB #BF-F3) (developed by S. Schiaffino, obtained from DSHB) in combination with AffiniPure goat anti-mouse IgG, Fc γ subclass 2b—DyLightTM405 (111-475-207), goat anti-mouse IgG, Fc γ subclass 1—Alexa Fluor[®] 488(115-545-205), and goat anti-mouse IgM μ chain—Alexa Fluor[®] 594 (115-585-075; Jackson ImmunoResearch) were used. Tissues were snap-frozen on liquid nitrogen, and 10 μ m cryosections were mounted on Superfrost ultra plus slides (Thermo Scientific #J3800AMNZ). Tissue sections were dried at RT, fixed with 4% PFA/0.1% sodium-deoxycholate/0.02% NP-40/PBS for 5 min, washed 3 times with PBS, and blocked in 2% FCS, 0.5% NP-40/PBS for 1 h. Sections were incubated with primary antibodies (1:100) overnight at 4°C, washed three times with PBS, and incubated with secondary antibodies (1:500), followed by washing three times with PBS and embedding in Fluoromount W (Serva #21634.01).

Transmission electron microscopy

Tissues were fixed by perfusion with 1.5% paraformaldehyde, 1.5% glutaraldehyde, and 0.15 M HEPES and were kept in fixative for at least 24 h at 4°C. Thereafter, tissue was fixed in 1% osmium tetroxide solution (Sigma #75633) and incubated in uranyl-acetate (Agar Scientific #AGR1260A). Tissues were dehydrated in an ascending series of ethanol and embedded in Agar 100 Resin (Agar Scientific #AGR1031). Muscles were sectioned using an ultra-microtome and analyzed using a TEM Zeiss EM 902 and Zeiss LEO 906.

Fluorescence-activated cell sorting (FACS)-based MuSC isolation and culture

Skeletal muscle tissue was dissected from individual mice and transferred into DMEM (Thermo#31966-021) containing 2% penicillin–streptomycin (Sigma #P0781-100 ml). The tissue was minced using a McIlwain Tissue Chopper (TC752), and tissue debris was removed by brief centrifugation (1 min, 1,200 g). The supernatant was digested with occasional vortexing using Dispase (BD #354-235; 1:10 in solution) for 30 min, followed by Collagenase II digestion (Worthington # LS004185; 1:10 in solution) for 30 min. Thereafter, fetal calf serum (Sigma-Aldrich #F7524-500ML, 10% f.c.) was added to the suspension. The cell suspensions were filtered using 100 μ m, 70 μ m, and 40 μ m cell EASYstrainer (Greiner#54200, 542070 and 542040), and cells were collected by centrifugation (5 min, 1,200 g). Cells were incubated in 200 μ l cell sorting buffer (CSB: 1 \times PBS, 1 mM EDTA, 25 mM HEPES pH7.0, 1% FCS) containing anti-CD45-APC, anti-CD31-APC, and anti-Ly-6A/E (Sca-1)-APC antibodies (eBioscience #17-0451, 17-0311, 17-5981, 1:100 each) for 30 min at 4°C. Cell suspensions originating from mice without ZsGreen marker gene expression were incubated for one hour with anti-CD45-APC, anti-CD31-APC, and anti-Ly-6A/E (Sca-1)-APC and additionally with anti-CD34-Alexa 450 (eBioscience #48-0311-80; 1:100) and anti-integrin-FITC (MBL #K0046-4; 1:100) antibodies. Cells were washed, centrifuged (5 min, 1,200 g), and re-suspended in 200 μ l CBS containing 30 μ l anti-APC MicroBeads (Miltenyi #130-090-855) for 20 min at 4°C. CSB, CD31, CD45, and Sca-1-positive cells were depleted using the Miltenyi AutoMACS. Pax7-ZsGreen-labeled

MuSCs were stained with DAPI (Invitrogen, #D1306), and samples with antibody labeling were stained with propidium iodide (Sigma-Aldrich, #P4864-10ML) to allow identification of dead cells. FACS sorting was done using a BD Aria III. Debris and clumps were excluded using forward and side scatter parameters. Dead cells were excluded using DAPI/PI, and residual APC-positive cells were excluded. Pax7-ZsGreen-labeled cells were analyzed and sorted using 488 nm excitation and emission at 530/30 nm. Antibody labeled MSCs were isolated based on co-detection of CD34-Alexa 450 (ex. 405 nm, em 450/40 nm) and Integrin-FITC (ex. 488 nm, em: 530/30 nm) signals. Isolated cells were cultured on Matrigel (Fisher # CB356238) covered dishes in proliferation medium (DMEM + GlutaMAX[™] #31966-021, 20% FCS, 2% PS). Cells were seeded at a density of 6,000 cells/cm². Half of the medium was exchanged every 2 days. Upon confluence, medium was exchanged to differentiation medium (DMEM 4.5% Glucose; 2% horse serum, Thermo Scientific #16050130; 1% Pen/Strep/Glutamine).

Analysis of cell confluence

Confluence of MuSCs during proliferation and differentiation was determined using an IncuCyte Zoom system (Essen BioScience). The basic analyzer tool was adjusted to segment satellite cells from background as recommended by the company's technical notes using representative phase contrast images. Conditions were set for a minimum area of 180 μ m² and a maximum of 5 \times 10⁷ μ m². Pictures of cells were taken at least every 3 h. MuSCs were cultured in clear bottom 96-well plates (Greiner #655090) as described above.

Knock-down experiments

For knock-down of Yy1 in activated MuSCs, isolated MuSCs were transfected with shRNAs against Yy1 (Sigma-Aldrich Mission shRNA library, clone#pLKO1#TRCN0000054555) 72 h after isolation of the MuSCs. Lipofectamine 3000 (Thermo#L3000015) was used according to the manufacturers' instructions. Cell confluence was monitored with the IncuCyte Zoom system for 95 h every 60 min as described. RNA was isolated using the miRNeasy Mini Kit (Qiagen #1038703). RT reaction and qPCR were done as described below using Yy1-specific oligonucleotides (TTCAGAATAATCAGGAGGT GAGTTC, GCGAGTTCTCGGTCACCATGTGGTC).

RNA isolation and cell fractionation

RNA was isolated from PBS-perfused tissues or cultured cells using the TRIZOL method according to the manufacturer's instructions. To separate nuclear and cytoplasmic RNA, C2C12 cells were grown to confluence on a 10-cm cell culture dish, washed twice with ice-cold PBS, and recovered in 1 ml PBS using a cell scraper. Cells were centrifuged at 1,000 g for 10 min, and the cell pellet was re-suspended in 200 μ l of cell lysis buffer (10 mM Tris pH 8.0, 140 mM NaCl, 1.5 mM MgCl₂, 0.5% NP-40). Re-suspended cells were kept on ice for 5 min, flicked from time to time, and centrifuged at 1,000 g for 3 min. The supernatant was recovered as cytoplasmic fraction. RNA was isolated from the cytoplasmic fraction after addition of 700 μ l of TRIZOL. The remaining pellet was re-suspended twice in cell lysis buffer followed by centrifugation for

3 min at 1,000 g and once using a wash buffer (cell lysis buffer with additional 1% Tween-40 and 0.5% deoxycholic acid). The remaining pellet, representing the nuclear fraction, was re-suspended in 700 μ l TRIzol, and RNA was isolated. In addition, a human tissue RNA collection (Clontech human total RNA master panel II cat#636643) was used for RT-PCR experiments.

Transcriptome analysis and RT-PCR

Quality of isolated RNAs was confirmed using the Agilent 2100 Bioanalyzer in combination with Agilent RNA 6000 Pico or Nano KIT. RNA isolated from *in vitro* cultured MuSCs was analyzed using the mouse Clariom™ D Pico Assay Kit. RNA isolated from mouse tissues was analyzed using the mouse Clariom D Assay Kit strictly following the manufacturer's protocols. Data were analyzed using the Affymetrix Expression Console 1.4 with sst-RMA and DNASTAR Arraystar15. Gene set enrichment analysis (Subramanian *et al*, 2005) was performed using default parameters with permutation type gene sets. The maximum gene set size was adjusted from 50 to 1,000. For (q)RT-PCR, RNA was reverse transcribed using Superscript II (Thermo# 18064-022) and gene-specific oligonucleotides were used to detect the transcripts (mmu-linc-MYH: GTGCAGC CAGAACAAGACAGACAGT, GTGGTAATTGTAGGTGGTGAGCAGA (GAGCTGGCAAAACATAGTCCCTTCT for qRT-PCR), hsa-linc-MYH: CATGGTCTTGACACTTTGAGGACTA, TTGCATAAATGAGTCCGAT GCACAG, hsa-/mmu-GAPDH, ACCACAGTCCATGCCATCAC, CAT GCCAGTGAGCTTCCCGT). For quantitative RT-PCR, the KAPA SYBR FAST kit (Kappa Biosystems #KK4618) was used together with the Applied Biosystems StepOnePlus real-time PCR system.

Immunoprecipitation of the INO80 complex

For immunoprecipitation, protein extracts were prepared from TA muscle of WT and linc-MYH KO mice or from INO80-V5 and linc-MYH KO/INO80-V5 animals. Isolated TA muscle was frozen in liquid nitrogen until further use. Tissue was disrupted by the Covaris cryoPREP™ Extraction System (cryoPREP™ CP02) using the Tissuetube™ (#TT05) and three times maximum power disruption. The sample was transferred into an Eppendorf tube with 10 μ l/mg tissue RIPA buffer (50 mM Tris-HCl pH 7.4, 1% NP-40, 0.25% sodium-deoxycholate, 150 mM NaCl, 1 \times Protease Inhibitor Cocktail III (Merck#539134)) and was homogenized using a Ultrasonic Homogenizer (Bandelin Sonopuls with MS72 probe) using cycle 5, 30% power for 30 s. The lysate was incubated at 4°C on a rotating wheel for 30 min, followed by a 20,000 rcf centrifugation at 4°C for 20 min. The supernatant was stored as protein lysate at -80°C until further use. 60 μ l/sample G-Sepharose-beads (Millipore#P3296) was washed twice using 1 ml RIPA buffer, incubated in 1 ml 3% BSA (Sigma#A7284)/RIPA at 4°C on a rotating wheel for 1 h, washed twice using 1 ml of RIPA, and re-suspended in 60 μ l of RIPA. 1 ml of protein lysate (2 mg/ml) was incubated with 30 μ l bead suspension to scavenge proteins binding non-specifically to the beads at 4°C on a rotating wheel for 1 h. The supernatant was recovered and 10 μ g of anti-INO80 (Proteintech #18810-1-AP), or 4 μ g of anti-V5 antibody (Abcam #ab27671) was added, respectively. 30 μ l of blocked beads was added to the IP-mixture followed by incubation at 4°C on a rotating wheel overnight. Beads were washed

three times using 1 ml RIPA at 4°C on a rotating wheel for 10 min each time, and co-precipitated proteins were identified by mass spectrometry. For Western blot analysis, beads were re-suspended in Laemmli buffer at 95°C for 5 min and equal amounts of sample were used for analysis.

Western blot analysis

Muscle tissue of 6- to 25-week-old mice was lysed in RIPA buffer (50 mM Tris-HCl pH7.4, 150 mM NaCl, 1% NP-40, 0.25% Na-Deoxycholate, 1 \times cOmplete Protease Inhibitor cocktail, Roche #4693132001) by sonication. HEK 293 cells were lysed as described for the RNA-protein pull-down. 10–40 mg of protein extracts was separated using a 9% Bis-Tris SDS-PAGE for muscle tissue protein extracts and precast protein gels (Thermo #NBP0321BOX) for cellular protein extracts. Proteins were blotted onto nitrocellulose membranes. The following antibodies were used after blocking membranes with 3% BSA in TBS-T: Anti-RuvBl1 (1:1,000; Proteintech #10210-2-AP), anti-RuvBl2 (1:1,000; Bethyl #A302-536A), anti-TFPT (1:500; Proteintech#10097-2-AP), anti-WDR5 (1:1,000; Bethyl #A302-430A), anti-YY1 (1:1,000; Cell signaling #46395), RalA (1:5,000; Becton Dickinson #R23520), anti-V5 (1:5,000; Invitrogen #R960-25), and anti-FLAG (1:1,000, Sigma-Aldrich #F1804). Secondary antibodies were anti-mouse-HRP (1:5,000, Thermo #31450) and anti-rabbit-HRP (1:5,000, Thermo #31460).

In situ proximity ligation assay

The *in situ* proximity ligation assay (PLA) was performed on fixed primary proliferating MuSCs using the DuoLink PLA fluorescence technology (Sigma-Aldrich#DUO92101), following the manufacturer's protocol. About 2,000 isolated muscle satellite cells were seeded per well of a 96-well plate and grown to a confluence of about 80%. Cells were fixed using 4% PFA for 7 min at room temperature. Myoblasts were then permeabilized with 0.3% Triton X-100 in PBS three times for 5 min at room temperature. After two washing steps with PBS, cells were incubated with blocking solution in a humid chamber for 60 min at 37°C followed by incubation with primary antibodies for 1 h at room temperature. The assay was always performed with pairs of antibodies produced in mouse or rabbit, diluted 1:5,000 in antibody diluent. An anti-V5 tag antibody (Thermo Scientific; 37–7,500) recognizing the endogenous V5-tagged INO80 was used in combination with anti-YY1 (Cell Signaling#46395), anti-WDR5 (Bethyl#A302-429A), and anti-Ruvbl2 (Bethyl#A302-536A) antibodies, respectively. PLA probe incubation, ligation, and signal amplification were performed according to the manufacturer's protocol. After two washing steps with PBS, DAPI was diluted 1:5,000 in PBS and added to the cells for 5 min at room temperature.

RNA in situ hybridization-proximity ligation assay (rISH-PLA)

Interaction between linc-MYH and INO80 was confirmed using the rISH-PLA assay (Roussis *et al*, 2017). Five biotinylated 2'-O-Methyl RNA oligonucleotides against linc-MYH were designed using the Stellaris design tool (<https://www.biosearchtech.com/support/education/stellaris-rna-fish>): [Btn]GCCATTTGGTATACAGTCTGC[mA]

[mC][mG][mU], [Btn]CTCGTTGTCAAGTTCTGTATAGACCC[mA][mC][mG][mU], [Btn]CATTAGCTGTGGCTACATTA[mA][mG][mU][mC], [Btn]AGATTAGGGATGCTGCCTTG[mA][mC][mG][mU], [Btn]TGTCCTGGGGACTCAATAC[mA][mC][mG][mU]), anti-biotin antibody (Abcam #ab53494) and an anti-V5 tag antibody (Thermo Scientific; 37-7500) was used in the assay. The assay was performed as described using freshly isolated MuSCs grown on Greiner CELLSTAR® 96-well plates (Greiner #M0562-32EA) until the cells reached proliferating stage (72 h). The growth medium was removed, and the cells were fixed using 4% paraformaldehyde for seven minutes.

Mass spectrometry

For immunoaffinity precipitations, equal sample volumes were separated by polyacrylamide electrophoresis (NuPAGE 4–12% Bis-Tris gel, Thermo Fisher Scientific) prior to in-gel digestion (Shevchenko *et al*, 2006). Gel lanes were cut into seven blocks and diced finely. Gel-embedded proteins were subsequently reduced (10 mM dithiothreitol) and alkylated (55 mM iodoacetamide), followed by overnight digestion using trypsin (Serva). Peptides were gradually eluted from the gel by increasing concentrations of acetonitrile.

lncRNA-pull-downs were digested off-bead as follows: The pellet of magnetic beads was re-suspended in 6 M urea/2 M thiourea and proteins sequentially reduced (10 mM dithiothreitol) and alkylated (55 mM iodoacetamide) shaking at room temperature for 30 min, each. After a 3-h peptidolysis using 0.5 µg of Lys-C (Promega) with shaking at room temperature, samples were diluted four-fold with 100 mM triethylammonium bicarbonate. After addition of 0.5 µg trypsin (Serva), samples were incubated overnight while shaking, followed by magnetic removal of the beads.

Peptides from both sample types were finally desalted, concentrated, and stored on stop and go extraction (STAGE) tips (Rappsilber *et al*, 2003). Samples were subsequently analyzed by liquid chromatography/tandem mass spectrometry (LC-MS²) using in-house packed reverse-phase column emitters (70 µm ID, 15 cm length, ReproSil-Pur 120 C18-AQ, 1.9 µm, Dr. Maisch GmbH) and a buffer system including 5% acetonitrile, 0.1% formic acid, and 80% acetonitrile, 0.1% formic acid. Peptide/spectrum matching, protein group assembly, false discovery rate control (1% on the peptide and protein group level, both), and label-free quantitation were performed using the MaxQuant suite of algorithms (Cox & Mann, 2008; Cox *et al*, 2014) (IP: v. 1.6.1.0; lncRNA: v. 1.6.3.4) against the murine UniProt database (canonical and isoforms; IP: downloaded on 2018/02/09, 83082 entries; lncRNA downloaded on 2019/08/19, 86161 entries).

Analysis of IP data was done using a limma-based (Ritchie *et al*, 2015) in-house R pipeline (<https://github.com/bhagwataditya/autonomics>), including differential expression analysis and over-representation against gene ontology categories analysis using a Fisher exact test against the detectome. Only GO terms related to cellular components located in the nucleus were considered. Gene sets > 500 were excluded from the analysis to exclude general categories. RNA–protein pull-down data were analyzed by gene set enrichment analysis using the GESA tool (Subramanian *et al*, 2005). The summarized detectome of all RNA–protein pull-down samples was used to generate the reference *.chip-file. Enrichment analysis was applied to LFQ intensities of detected proteins. The Molecular

Signatures Database (MSigDB) GO.all.v7.0.symbols.gmt gene sets were employed, with default settings except permutation type set to gene_set and using classic enrichment statistics. Results were filtered for gene sets with FDR $P < 0.05$ and for gene sets related to nuclear functions.

Quantification and statistical analysis

ImageJ was used for quantification of fiber cross-sectional areas using the wand tool with manual correction of misalignments. Investigators were blinded for different samples. Data containing replicate values were tested for Gaussian distribution of values using GraphPad PRISM 6. All data are presented as mean ± SEM. When normality of the data was confirmed, Student's *t*-test was used as indicated in the legends. When normal distribution of data was not demonstrated, non-parametric statistical tests were used.

Data availability

Microarray data are available at Arrayexpress (E-MTAB-8592; <https://www.ebi.ac.uk/arrayexpress/experiments/E-MTAB-8592/>).

Expanded View for this article is available online.

Acknowledgements

We would like to thank Sylvia Thomas, Kerstin Richter, Susanne Kreutzer, Sonja Krueger, Alica Klaus, and Silvia Jeratsch for technical assistance. We thank Shuichi Watanabe for support with immunofluorescence protocols, Ulrich Gärtner, and Gerhard Kripp for electron microscopy. The comments of Shuichi Watanabe and Johnny Kim on the manuscript are greatly appreciated. This work was supported by the Max-Planck-Society, the LOEWE network “Medical RNomics”, the DFG RTG 2355, TRR267, and TRR81. Open access funding enabled and organized by Projekt DEAL.

Author contributions

CS and TBo conceived and performed experiments. AH, SH, IK, MV, and JG performed experiments. AA optimized the sample preparation and cell sorting protocols. CS, TBr, and TBo wrote the manuscript. TBr and TBo secured funding.

Conflict of interest

The authors declare that they have no conflict of interest.

References

- Abmayr SM, Pavlath GK (2012) Myoblast fusion: lessons from flies and mice. *Development* 139: 641–656
- Adams DJ, Quail MA, Cox T, van der Weyden L, Gorick BD, Su Q, Chan WI, Davies R, Bonfield JK, Law F *et al* (2005) A genome-wide, end-sequenced 129Sv BAC library resource for targeting vector construction. *Genomics* 86: 753–758
- Almada AE, Wagers AJ (2016) Molecular circuitry of stem cell fate in skeletal muscle regeneration, ageing and disease. *Nat Rev Mol Cell Biol* 17: 267–279
- Aramayo RJ, Willhoft O, Ayala R, Bythell-Douglas R, Wigley DB, Zhang X (2018) Cryo-EM structures of the human INO80 chromatin-remodeling complex. *Nat Struct Mol Biol* 25: 37–44

- Ayala R, Willhoft O, Aramayo RJ, Wilkinson M, McCormack EA, Ocloo L, Wigley DB, Zhang X (2018) Structure and regulation of the human INO80-nucleosome complex. *Nature* 556: 391–395
- Baghdadi MB, Tajbakhsh S (2018) Regulation and phylogeny of skeletal muscle regeneration. *Dev Biol* 433: 200–209
- Begus-Nahrman Y, Lechel A, Obenauf AC, Nalapareddy K, Peit E, Hoffmann E, Schlaudraff F, Liss B, Schirmacher P, Kestler H *et al* (2009) p53 deletion impairs clearance of chromosomal-instable stem cells in aging telomere-dysfunctional mice. *Nat Genet* 41: 1138–1143
- Boonsanay V, Zhang T, Georgieva A, Kostin S, Qi H, Yuan X, Zhou Y, Braun T (2016) Regulation of skeletal muscle stem cell quiescence by Suv4-20h1-dependent facultative heterochromatin formation. *Cell Stem Cell* 18: 229–242
- Bosnakovski D, Xu Z, Li W, Thet S, Cleaver O, Perlingeiro RC, Kyba M (2008) Prospective isolation of skeletal muscle stem cells with a Pax7 reporter. *Stem Cells* 26: 3194–3204
- Bozek K, Wei Y, Yan Z, Liu X, Xiong J, Sugimoto M, Tomita M, Paabo S, Pieszek R, Sherwood CC *et al* (2014) Exceptional evolutionary divergence of human muscle and brain metabolomes parallels human cognitive and physical uniqueness. *PLoS Biol* 12: e1001871
- Brahma S, Ngubo M, Paul S, Udugama M, Bartholomew B (2018) The Arp8 and Arp4 module acts as a DNA sensor controlling INO80 chromatin remodeling. *Nat Commun* 9: 3309
- Cabili MN, Trapnell C, Goff L, Koziol M, Tazon-Vega B, Regev A, Rinn JL (2011) Integrative annotation of human large intergenic noncoding RNAs reveals global properties and specific subclasses. *Genes Dev* 25: 1915–1927
- Cai Y, Jin J, Yao T, Gottschalk AJ, Swanson SK, Wu S, Shi Y, Washburn MP, Florens L, Conaway RC *et al* (2007) YY1 functions with INO80 to activate transcription. *Nat Struct Mol Biol* 14: 872–874
- Cai Y, Jin J, Swanson SK, Cole MD, Choi SH, Florens L, Washburn MP, Conaway JW, Conaway RC (2010) Subunit composition and substrate specificity of a MOF-containing histone acetyltransferase distinct from the male-specific lethal (MSL) complex. *J Biol Chem* 285: 4268–4272
- Cao L, Ding J, Dong L, Zhao J, Su J, Wang L, Sui Y, Zhao T, Wang F, Jin J *et al* (2015) Negative regulation of p21Waf1/Cip1 by human INO80 chromatin remodeling complex is implicated in cell cycle phase G2/M arrest and abnormal chromosome stability. *PLoS ONE* 10: e0137411
- Caretto G, Di Padova M, Micales B, Lyons GE, Sartorelli V (2004) The Polycomb Ezh2 methyltransferase regulates muscle gene expression and skeletal muscle differentiation. *Genes Dev* 18: 2627–2638
- Carlevaro-Fita J, Johnson R (2019) Global positioning system: understanding long noncoding RNAs through subcellular localization. *Mol Cell* 73: 869–883
- Chen L, Cai Y, Jin J, Florens L, Swanson SK, Washburn MP, Conaway JW, Conaway RC (2011) Subunit organization of the human INO80 chromatin remodeling complex: an evolutionarily conserved core complex catalyzes ATP-dependent nucleosome remodeling. *J Biol Chem* 286: 11283–11289
- Chen F, Zhou J, Li Y, Zhao Y, Yuan J, Cao Y, Wang L, Zhang Z, Zhang B, Wang CC *et al* (2019) YY1 regulates skeletal muscle regeneration through controlling metabolic reprogramming of satellite cells. *EMBO J* 38: e99727
- Cox J, Mann M (2008) MaxQuant enables high peptide identification rates, individualized p.p.b.-range mass accuracies and proteome-wide protein quantification. *Nat Biotechnol* 26: 1367–1372
- Cox J, Hein MY, Luber CA, Paron I, Nagaraj N, Mann M (2014) Accurate proteome-wide label-free quantification by delayed normalization and maximal peptide ratio extraction, termed MaxLFQ. *Mol Cell Proteomics* 13: 2513–2526
- Das DK, Graham ZA, Cardozo CP (2019) Myokines in skeletal muscle physiology and metabolism: recent advances and future perspectives. *Acta Physiol (Oxf)* 228: e13367
- Dias J, Van Nguyen N, Georgiev P, Gaub A, Brettschneider J, Cusack S, Kadlec J, Akhtar A (2014) Structural analysis of the KANSL1/WDR5/KANSL2 complex reveals that WDR5 is required for efficient assembly and chromatin targeting of the NSL complex. *Genes Dev* 28: 929–942
- Eustermann S, Schall K, Kostrewa D, Lakomek K, Strauss M, Moldt M, Hopfner KP (2018) Structural basis for ATP-dependent chromatin remodelling by the INO80 complex. *Nature* 556: 386–390
- Feige P, Brun CE, Ritso M, Rudnicki MA (2018) Orienting muscle stem cells for regeneration in homeostasis, aging, and disease. *Cell Stem Cell* 23: 653–664
- Fickett JW (1982) Recognition of protein coding regions in DNA sequences. *Nucleic Acids Res* 10: 5303–5318
- Flamini V, Ghadiali RS, Antczak P, Rothwell A, Turnbull JE, Pisconti A (2018) The satellite cell niche regulates the balance between myoblast differentiation and self-renewal via p53. *Stem Cell Reports* 10: 970–983
- Fukada SI (2018) The roles of muscle stem cells in muscle injury, atrophy and hypertrophy. *J Biochem* 163: 353–358
- Garcia-Prat L, Sousa-Victor P, Munoz-Canoves P (2013) Functional dysregulation of stem cells during aging: a focus on skeletal muscle stem cells. *FEBS J* 280: 4051–4062
- Gloss BS, Dinger ME (2016) The specificity of long noncoding RNA expression. *Biochim Biophys Acta* 1859: 16–22
- Hardy D, Besnard A, Latil M, Jouvion G, Briand D, Thepenier C, Pascal Q, Guguin A, Gayraud-Morel B, Cavaillon JM *et al* (2016) Comparative study of injury models for studying muscle regeneration in mice. *PLoS ONE* 11: e0147198
- Jaiswal PK, Koul S, Shanmugam PST, Koul HK (2018) Eukaryotic translation initiation factor 4 gamma 1 (eIF4G1) is upregulated during Prostate cancer progression and modulates cell growth and metastasis. *Sci Rep* 8: 7459
- Kang YJ, Yang DC, Kong L, Hou M, Meng YQ, Wei L, Gao G (2017) CPC2: a fast and accurate coding potential calculator based on sequence intrinsic features. *Nucleic Acids Res* 45: W12–W16
- Kashiwaba S, Kitahashi K, Watanabe T, Onoda F, Ohtsu M, Murakami Y (2010) The mammalian INO80 complex is recruited to DNA damage sites in an ARP8 dependent manner. *Biochem Biophys Res Commun* 402: 619–625
- Keefe AC, Lawson JA, Flygare SD, Fox ZD, Colasanto MP, Mathew SJ, Yandell M, Kardon G (2015) Muscle stem cells contribute to myofibres in sedentary adult mice. *Nat Commun* 6: 7087
- Keller C, Hansen MS, Coffin CM, Capecchi MR (2004) Pax3: Fkhr interferes with embryonic Pax3 and Pax7 function: implications for alveolar rhabdomyosarcoma cell of origin. *Genes Dev* 18: 2608–2613
- Kong L, Zhang Y, Ye ZQ, Liu XQ, Zhao SQ, Wei L, Gao G (2007) CPC: assess the protein-coding potential of transcripts using sequence features and support vector machine. *Nucleic Acids Res* 35: W345–W349
- Kopp F, Mendell JT (2018) Functional classification and experimental dissection of long noncoding RNAs. *Cell* 172: 393–407
- Lee SA, Lee HS, Hur SK, Kang SW, Oh GT, Lee D, Kwon J (2017) INO80 haploinsufficiency inhibits colon cancer tumorigenesis via replication stress-induced apoptosis. *Oncotarget* 8: 115041–115053
- Liu Y, Elf SE, Miyata Y, Sashida G, Liu Y, Huang G, Di Giandomenico S, Lee JM, Deblasio A, Menendez S *et al* (2009) p53 regulates hematopoietic stem cell quiescence. *Cell Stem Cell* 4: 37–48

- Liu L, Charville GW, Cheung TH, Yoo B, Santos PJ, Schroeder M, Rando TA (2018) Impaired notch signaling leads to a decrease in p53 activity and mitotic catastrophe in aged muscle stem cells. *Cell Stem Cell* 23: 544–556.e4
- Machado L, Esteves de Lima J, Fabre O, Proux C, Legendre R, Szegedi A, Varet H, Ingerslev LR, Barres R, Relaix F et al (2017) *In situ* fixation redefines quiescence and early activation of skeletal muscle stem cells. *Cell Rep* 21: 1982–1993
- Marroncelli N, Bianchi M, Bertin M, Consalvi S, Saccone V, De Bardi M, Puri PL, Palacios D, Adamo S, Moresi V (2018) HDAC4 regulates satellite cell proliferation and differentiation by targeting P21 and Sharp1 genes. *Sci Rep* 8: 3448
- Mauro A (1961) Satellite cell of skeletal muscle fibers. *J Biophys Biochem Cytol* 9: 493–495
- Min JN, Tian Y, Xiao Y, Wu L, Li L, Chang S (2013) The INO80 chromatin remodeling complex is required for efficient telomere replication and maintenance of genome stability. *Cell Res* 23: 1396–1413
- Moore JW, Dionne C, Jaye M, Swain JL (1991) The mRNAs encoding acidic FGF, basic FGF and FGF receptor are coordinately downregulated during myogenic differentiation. *Development* 111: 741–748
- Moran VA, Niland CN, Khalil AM (2012) Co-Immunoprecipitation of long noncoding RNAs. In *Methods Mol Biol*, Engel N (ed.) pp 219–228. Cham: Springer Nature
- Morrison AJ (2017) Genome maintenance functions of the INO80 chromatin remodeller. *Philos Trans R Soc Lond B Biol Sci* 372: 20160289
- Motohashi N, Asakura A (2014) Muscle satellite cell heterogeneity and self-renewal. *Front Cell Dev Biol* 2: 1
- Murach KA, White SH, Wen Y, Ho A, Dupont-Versteegden EE, McCarthy JJ, Peterson CA (2017) Differential requirement for satellite cells during overload-induced muscle hypertrophy in growing versus mature mice. *Skelet Muscle* 7: 14
- Murphy MM, Lawson JA, Mathew SJ, Hutcheson DA, Kardon G (2011) Satellite cells, connective tissue fibroblasts and their interactions are crucial for muscle regeneration. *Development* 138: 3625–3637
- Oustanina S, Hause G, Braun T (2004) Pax7 directs postnatal renewal and propagation of myogenic satellite cells but not their specification. *EMBO J* 23: 3430–3439
- Pawlikowski B, Pulliam C, Betta ND, Kardon G, Olwin BB (2015) Pervasive satellite cell contribution to uninjured adult muscle fibers. *Skelet Muscle* 5: 42
- Pawlikowski B, Vogler TO, Gadek K, Olwin BB (2017) Regulation of skeletal muscle stem cells by fibroblast growth factors. *Dev Dyn* 246: 359–367
- Poli J, Gasser SM, Papamichos-Chronakis M (2017) The INO80 remodeller in transcription, replication and repair. *Philos Trans R Soc Lond B Biol Sci* 372: 20160290
- Qiu Z, Elsayed Z, Peterkin V, Alkatib S, Bennett D, Landry JW (2016) Ino80 is essential for proximal-distal axis asymmetry in part by regulating Bmp4 expression. *BMC Biol* 14: 18
- Quinn JJ, Chang HY (2015) Unique features of long non-coding RNA biogenesis and function. *Nat Rev Genet* 17: 47–62
- Ramirez-Valle F, Braunstein S, Zavadil J, Formenti SC, Schneider RJ (2008) eIF4G1 links nutrient sensing by mTOR to cell proliferation and inhibition of autophagy. *J Cell Biol* 181: 293–307
- Ran FA, Hsu PD, Wright J, Agarwala V, Scott DA, Zhang F (2013) Genome engineering using the CRISPR-Cas9 system. *Nat Protoc* 8: 2281–2308
- Rappasilber J, Ishihama Y, Mann M (2003) Stop and go extraction tips for matrix-assisted laser desorption/ionization, nanoelectrospray, and LC/MS sample pretreatment in proteomics. *Anal Chem* 75: 663–670
- Ritchie ME, Phipson B, Wu D, Hu Y, Law CW, Shi W, Smyth GK (2015) limma powers differential expression analyses for RNA-sequencing and microarray studies. *Nucleic Acids Res* 43: e47
- Robinson DCL, Dilworth FJ (2018) Epigenetic regulation of adult myogenesis. *Curr Top Dev Biol* 126: 235–284
- Rodriguez CI, Buchholz F, Galloway J, Sequerra R, Kasper J, Ayala R, Stewart AF, Dymecki SM (2000) High-efficiency deleter mice show that FLP is an alternative to Cre-loxP. *Nat Genet* 25: 139–140
- Roussis IM, Myers FA, Scarlett GP (2017) RNA whole-mount *in situ* hybridization proximity ligation assay (rISH-PLA), an assay for detecting RNA-protein complexes in intact cells. *Curr Protoc Cell Biol* 74: 17.20.1–17.20.10
- Runge JS, Raab JR, Magnuson T (2018) Identification of two distinct classes of the human INO80 complex genome-wide. *G3: Genes - Genomes - Genetics* 8: 1095–1102
- Sakakibara I, Santolini M, Ferry A, Hakim V, Maire P (2014) Six homeoproteins and a linc-RNA at the fast MYH locus lock fast myofiber terminal phenotype. *PLoS Genet* 10: e1004386
- Schuelke M, Wagner KR, Stolz LE, Hubner C, Riebel T, Komen W, Braun T, Tobin JF, Lee SJ (2004) Myostatin mutation associated with gross muscle hypertrophy in a child. *N Engl J Med* 350: 2682–2688
- Schweisguit J, Schutt C, Wust S, Wietelmann A, Ghesquiere B, Carmeliet P, Drose S, Korach KS, Braun T, Boettger T (2017) Sex-specific, reciprocal regulation of ERalpha and miR-22 controls muscle lipid metabolism in male mice. *EMBO J* 36: 1199–1214
- Seale P, Sabourin LA, Giris-Gabardo A, Mansouri A, Gruss P, Rudnicki MA (2000) Pax7 is required for the specification of myogenic satellite cells. *Cell* 102: 777–786
- Segales J, Perdiguero E, Munoz-Canoves P (2016) Regulation of muscle stem cell functions: a focus on the p38 MAPK signaling pathway. *Front Cell Dev Biol* 4: 91
- Shevchenko A, Tomas H, Havlis J, Olsen JV, Mann M (2006) In-gel digestion for mass spectrometric characterization of proteins and proteomes. *Nat Protoc* 1: 2856–2860
- Subramanian A, Tamayo P, Mootha VK, Mukherjee S, Ebert BL, Gillette MA, Paulovich A, Pomeroy SL, Golub TR, Lander ES et al (2005) Gene set enrichment analysis: a knowledge-based approach for interpreting genome-wide expression profiles. *Proc Natl Acad Sci USA* 102: 15545–15550
- Tosi A, Haas C, Herzog F, Gilmozzi A, Berninghausen O, Ungewickell C, Gerhold CB, Lakomek K, Aebersold R, Beckmann R et al (2013) Structure and subunit topology of the INO80 chromatin remodeler and its nucleosome complex. *Cell* 154: 1207–1219
- Ulitsky I, Bartel DP (2013) lincRNAs: genomics, evolution, and mechanisms. *Cell* 154: 26–46
- Vassileva I, Yanakieva I, Peycheva M, Gospodinov A, Anachkova B (2014) The mammalian INO80 chromatin remodeling complex is required for replication stress recovery. *Nucleic Acids Res* 42: 9074–9086
- Vella P, Barozzi I, Cuomo A, Bonaldi T, Pasini D (2012) Yin Yang 1 extends the Myc-related transcription factors network in embryonic stem cells. *Nucleic Acids Res* 40: 3403–3418
- van Velthoven CTJ, de Morree A, Egner IM, Brett JO, Rando TA (2017) Transcriptional profiling of quiescent muscle stem cells *in vivo*. *Cell Rep* 21: 1994–2004
- van Velthoven CTJ, Rando TA (2019) Stem cell quiescence: dynamism, restraint, and cellular idling. *Cell Stem Cell* 24: 213–225
- Wang L, Du Y, Ward JM, Shimbo T, Lackford B, Zheng X, Miao YL, Zhou B, Han L, Fargo DC et al (2014) INO80 facilitates pluripotency gene activation in embryonic stem cell self-renewal, reprogramming, and blastocyst development. *Cell Stem Cell* 14: 575–591

- Wang M, Liu C, Su Y, Zhang K, Zhang Y, Chen M, Ge M, Gu L, Lu T, Li N et al (2017) miRNA-34c inhibits myoblasts proliferation by targeting YY1. *Cell Cycle* 16: 1661–1672
- Warming S, Costantino N, Court DL, Jenkins NA, Copeland NG (2005) Simple and highly efficient BAC recombineering using galK selection. *Nucleic Acids Res* 33: e36
- White RB, Bierinx AS, Gnocchi VF, Zammit PS (2010) Dynamics of muscle fibre growth during postnatal mouse development. *BMC Dev Biol* 10: 21
- Woodhouse S, Pugazhendhi D, Brien P, Pell JM (2013) Ezh2 maintains a key phase of muscle satellite cell expansion but does not regulate terminal differentiation. *J Cell Sci* 126: 565–579
- Wosczyzna MN, Rando TA (2018) A muscle stem cell support group: coordinated cellular responses in muscle regeneration. *Dev Cell* 46: 135–143
- Wu S, Shi Y, Mulligan P, Gay F, Landry J, Liu H, Lu J, Qi HH, Wang W, Nickoloff JA et al (2007) A YY1-INO80 complex regulates genomic stability through homologous recombination-based repair. *Nat Struct Mol Biol* 14: 1165–1172
- Wust S, Drose S, Heidler J, Wittig I, Klockner I, Franko A, Bonke E, Gunther S, Gartner U, Boettger T et al (2018) Metabolic maturation during muscle stem cell differentiation is achieved by miR-1/133a-mediated inhibition of the Dlk1-Dio3 mega gene cluster. *Cell Metab* 27: 1026–1039.e6
- Yakovleva T, Kolesnikova L, Vukojevic V, Gileva I, Tan-No K, Austen M, Luscher B, Ekstrom TJ, Terenius L, Bakalkin G (2004) YY1 binding to a subset of p53 DNA-target sites regulates p53-dependent transcription. *Biochem Biophys Res Commun* 318: 615–624
- Yamaguchi M, Watanabe Y, Ohtani T, Uezumi A, Mikami N, Nakamura M, Sato T, Ikawa M, Hoshino M, Tsuchida K et al (2015) Calcitonin receptor signaling inhibits muscle stem cells from escaping the quiescent state and the niche. *Cell Rep* 13: 302–314
- Zhang T, Gunther S, Looso M, Kunne C, Kruger M, Kim J, Zhou Y, Braun T (2015) Prmt5 is a regulator of muscle stem cell expansion in adult mice. *Nat Commun* 6: 7140
- Zhou C, Zou J, Zou S, Li X (2016) INO80 is required for osteogenic differentiation of human mesenchymal stem cells. *Sci Rep* 6: 35924



License: This is an open access article under the terms of the Creative Commons Attribution-NonCommercial-NoDerivs 4.0 License, which permits use and distribution in any medium, provided the original work is properly cited, the use is non-commercial and no modifications or adaptations are made.